Volume 180 Number 8 September 2007

JOURNAL OF SOLID STATE CHEMISTRY

Review Article

Recent rare-earth multinuclear clusters and rare-earth coordination polymers based on $[Ln_2(\mu_2\text{-}H_2O)_2(RCO_2)_4]$ (Ln = rare-earth metal and R = aromatic or aliphatic)

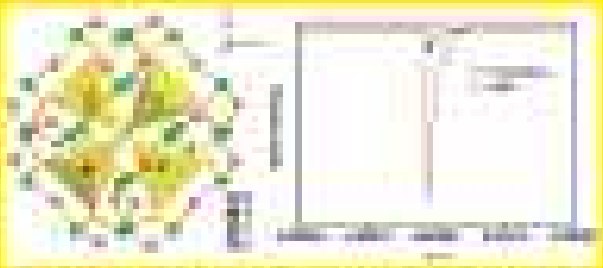

Wenbing Dou, Xiaofei Li, Wei-Dong Fu, Hongjun Suen, Hong-Ping Xia

Available online at ScienceDirect

Journal of Solid State Chemistry
Supports *open access*

4.1 CiteScore | 2.726 Impact Factor

Submit your article Guide for Authors

Latest issue All issues •••

Search in this journal

About the journal

Aims and scope Editorial board Abstracting and indexing

Editor-in-Chief

Associate Editors

Editorial Board

Journal of Solid State Chemistry

Supports *open access*

4.1
CiteScore

Volume 292

December 2020

Download full issue

Previous vol/issue Next vol/issue

Full text access

Editorial Board

Article 121809

Download PDF

Regular Articles

Research article ○ Abstract only

A 3D supramolecular photo-/ electro-catalytic material based on 2D monoarsenate capped Dawson layer and metal-organic sheets with rich π–π interactions

Yu-Hang Guo, Li-Ping Cui, Jing-Hua Lv, Kai Yu, ... Bai-Bin Zhou

Article 121605

Purchase PDF Article preview

Abstract Graphical abstract

Graphical abstract

Journal of Solid State Chemistry

Supports *open access*

4.1
CiteScore

Research article ○ Abstract only

Eco-friendly mechanochemical intercalation of imidazole into kaolinite

Breidi Albach, Marcus V. Liz, Liziê D.T. Prola, Ronilson V. Barbosa, ... Daniel S. Rampon

Article 121649

Purchase PDF Article preview

Abstract Graphical abstract

Graphical abstract

A hybrid organic-inorganic material was prepared by mechanochemical intercalation of imidazole into low-defect kaolinite using a simple solvent-free methodology without previous intercalation steps.

Research article ○ Abstract only

Electrochemical alloying/dealloying mechanism of ternary intermetallic $Cu_{6-\delta}Zn_{2+\delta}Sb_2$ ($\delta = 0$ and 1) as anode for Li-ion and Na-ion batteries

Debanjana Pahari, Samiran Misra, Partha P. Jana, Sreeraj Puravankara

Article 121660

Purchase PDF Article preview

Abstract Graphical abstract

Graphical abstract

Novel ternary intermetallic $Cu_{6-\delta}Zn_{2+\delta}Sb_2$ ($\delta = 0$ and 1) with unique mechanism for lithium and sodium alloying/dealloying reactions.

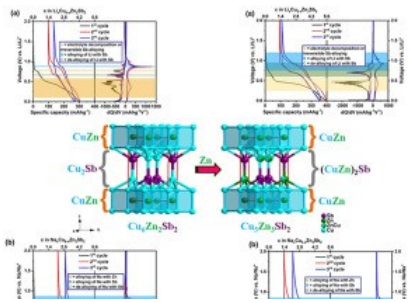

Journal of Solid State Chemistry
Supports *open access*

4.1
CiteScore

Defect properties of $Bi_{12}SiO_{12}$ and $Bi_4Si_3O_{12}$ compounds.

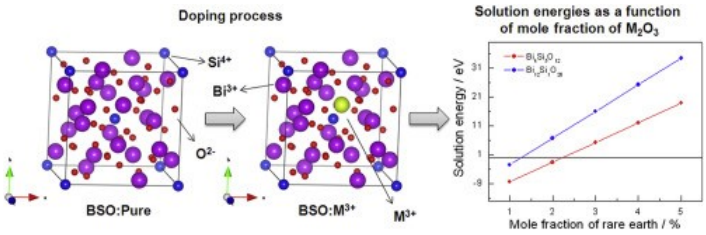

Research article ○ Abstract only

Aptamer-functionalized Fe_3O_4@MOF nanocarrier for targeted drug delivery and fluorescence imaging of the triple-negative MDA-MB-231 breast cancer cells

Hamed Alijani, Abolhassan Noori, Nassim Faridi, S.Zahra Bathaie, Mir F. Mousavi
Article 121680

Purchase PDF Article preview

Abstract Graphical abstract

Graphical abstract

We prepared Fe_3O_4@UiO-66-NH_2 MOF shell nanocarriers. The nanocarriers were loaded with DOX as well as fluorescent carbon dots and were capped with the nucleolin aptamer. The multi-stimuli-responsive nanocarriers demonstrated excellent cytotoxicity to the triple-negative MDA-MB-231 breast cancer cells cancer cell, and were used for cell imaging as well.

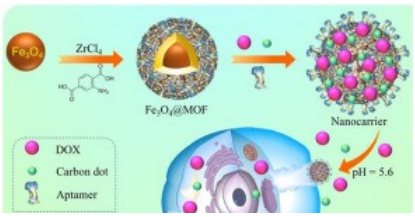

Research article ○ Abstract only

Preparation of egg white@zeolitic imidazolate framework-8@polyacrylic acid aerogel and its adsorption properties for organic dyes

Qingqing Wang, Liling Lei, Fangcao Wang, Congtao Chen, ... Zhijun Chen
Article 121656

Purchase PDF Article preview

Abstract Graphical abstract

Journal of Solid State Chemistry
Supports *open access*

4.1
CiteScore

Research article ○ Abstract only

High lithium ionic conductivity of γ-Li_3PO_4-type solid electrolytes in Li_4GeO_4–Li_4SiO_4–Li_3VO_4 quasi-ternary system

Guowei Zhao, Kota Suzuki, Tomoaki Seki, Xueying Sun, ... Ryoji Kanno

Article 121651

Purchase PDF Article preview

Abstract Graphical abstract

Graphical abstract

γ-Li_3PO_4-type lithium ionic conductors with high lithium ionic conductivity were synthesized and examined as a solid-electrolyte in the Li_4GeO_4–Li_4SiO_4–Li_3VO_4 ternary system.

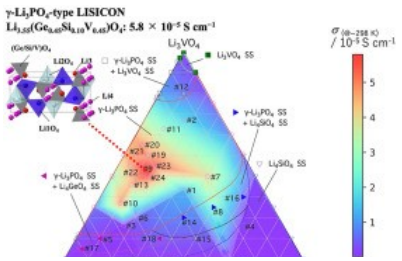

Research article ○ Abstract only

Synthesis, crystal structure and characterization of monocrystalline $ZnCr_2Se_4$ doped with neodymium

Izabela Jendrzejewska, Tadeusz Groń, Joachim Kusz, Zoia Barsova, ... Henryk Duda

Article 121661

Purchase PDF Article preview

Abstract Graphical abstract

Graphical abstract

The ($Zn_{1-x}Nd_xCr_2Se_4$) – single crystals obtained by chemical vapour transport and their physical properties.

Journal of Solid State Chemistry
Supports *open access*

4.1
CiteScore

Purchase PDF Article preview

Abstract Graphical abstract

Graphical abstract

Two new Mg(II)-Ln (III) (Ln = Eu, Tb) heterometallic coordination polymers with topology symbol of $\{4^4.6^2\}_3\{4^9.6^6\}_2$ were synthesized. They can reversibly transform into 0D complexes through single-crystal-to-single-crystal transformation in solution. They show characteristic emission spectra of Eu(III) or Tb(III) ions.

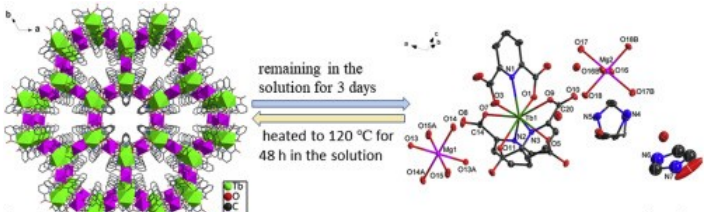

Research article ○ Abstract only

Phase diagram studies on ternary Bi–Mo–O system

P.M. Aiswarya, Sajal Ghosh, Rajesh Ganesan, T. Gnanasekaran

Article 121657

Purchase PDF Article preview

Abstract Graphical abstract

Graphical abstract

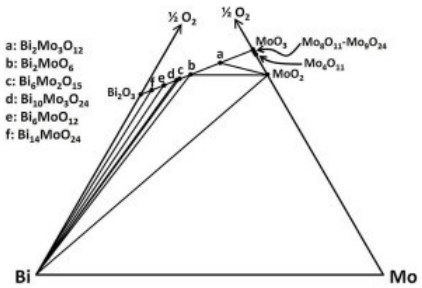

Research article ○ Abstract only

Microwave-assisted pressureless sintering of silicon-reinforced boron carbide composites

Boris Dyatkin, Raymond M. Gamache, Benjamin Y. Rock, Syed B. Qadri, ... Matthew Laskoski

Article 121659

Purchase PDF Article preview

Journal of Solid State Chemistry
Supports *open access*

4.1
CiteScore

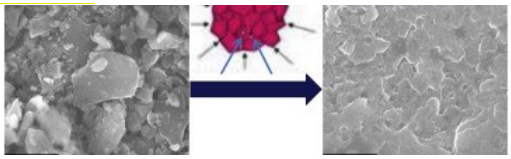

Research article ○ Abstract only

POM derived UOR and HER bifunctional NiS/MoS_2 composite for overall water splitting

Yang Zheng, Penghao Tang, Xinxin Xu, Xiaoguang Sang

Article 121644

Purchase PDF Article preview

Abstract Graphical abstract

Graphical abstract

NiS/MoS_2 "flower" was "planted" on functional carbon paper, which exhibits excellent UOR and HER properties in overall water splitting.

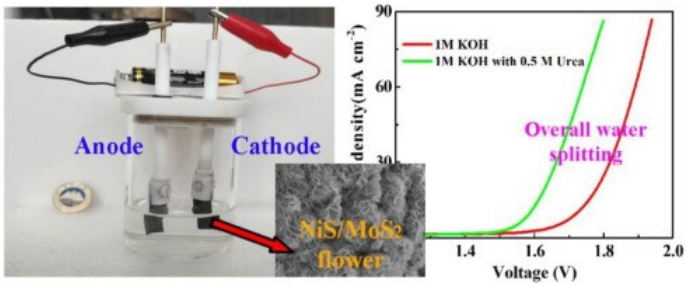

Research article ○ Abstract only

Enhancement of thermoelectric properties by partial substitution of Ge sites in anion ring $[Ge_2S_2]^{4-}$ found in $Co_2Ge_3S_3$ skutterudite-based material

Mi-Kyung Han, Sujin Kim, Sung-Jin Kim

Article 121590

Purchase PDF Article preview

Abstract Graphical abstract

Graphical abstract

The thermoelectric properties of skutterudite-type sulfide with various substitutional atoms are investigated. Partial substitution of Ge sites in anion rings $[Ge_2S_2]^{4-}$ found in $CoGe_{1.5}S_{1.5}$ suppresses the thermal transport (phonons). Compared with the referred $Co_2Ge_3S_3$ sample, the Bi-substituted skutterudite obtained the 21% reduction of the lattice thermal conductivity and 38% enhancement of power factor, resulting in a peak ZT value of ~0.22 at 763 K of $Co_2Ge_{2.97}Bi_{0.03}S_3$.

Journal of Solid State Chemistry
Supports *open access*

4.1
CiteScore

Article 121686

Purchase PDF Article preview

Abstract Graphical abstract

Graphical abstract

ZSM-5 zeolite (ZSM-5-SA) possesses mesopores and macropores via sodium alginate (SA) as template.

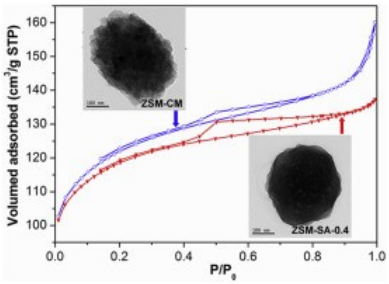

Research article ○ Abstract only

Coating BiOCl@g-C_3N_4 nanocomposite with a metal organic framework: Enhanced visible light photocatalytic activities

Yu Zhu, Min Zhu, Hua Lv, Suya Zhao, ... Bingdong Li

Article 121641

Purchase PDF Article preview

Abstract Graphical abstract

Graphical abstract

In this work, novel BiOCl/g-C_3N_4@UiO-66 composites were first prepared through the facile solvothermal approach via coating UiO-66 on the surface of BiOCl/g-C_3N_4. The materials exhibit higher RhB photocatalytic degradation under visible light irradiation, which can be attributed to the lower recombination probability of electron-hole pair of the heterojunction and increased surface area for RhB adsorption accomplished with during photodegradation process.

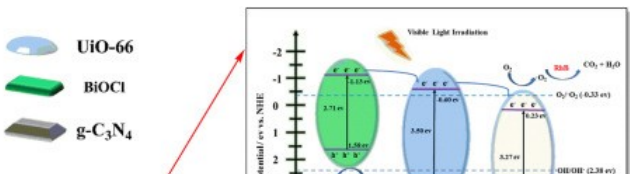

Research article ○ Abstract only

Structure and magnetism of a new hexagonal polymorph of $Ba_3Tb(BO_3)_3$ with a quasi-2D triangular lattice

Nicola D. Kelly, Cheng Liu, Siân E. Dutton

Article 121640

Journal of Solid State Chemistry
Supports *open access*

4.1
CiteScore

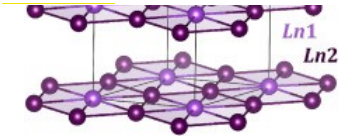

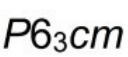

Research article ○ Abstract only

Structural diversity and near-infrared luminescence of lanthanide coordination polymers with different flexibility and coordination orientation based on bipyridyl carboxylate and dicarboxylate ligands

Lei Yan, Jun-Lin Zhang, Huai-Ming Hu, Fei Wang, ... Bo-Zhou Wang

Article 121654

Purchase PDF Article preview

Abstract Graphical abstract

Graphical abstract

Three series of new lanthanide coordination polymers have been synthesized under hydrothermal conditions. Compounds **1–10** exhibit variable structures with 2D and 3D when introduce aliphatic and aromatic dicarboxylates. The structural diversity of **1–10** indicates that coordination orientations of aromatic dicarboxylates have significant influence on the construction of coordination polymers.

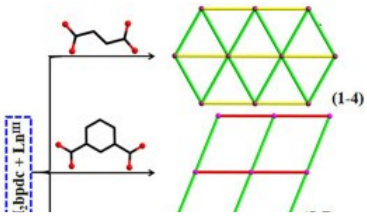

Research article ○ Abstract only

Cobalt oxide NPs immobilized on environmentally benign biological macromolecule-derived *N*-doped mesoporous carbon as an efficient catalyst for hydrogenation of nitroarenes

Zahra Soleimani Nanadegani, Firouzeh Nemati, Ali Elhampour, Yalda Rangraz

Article 121645

Purchase PDF Article preview

Abstract Graphical abstract

Graphical abstract

Journal of Solid State Chemistry
Supports *open access*

4.1
CiteScore

in aqueous system

Yongping Qu, Lingling Gao, Yujuan Zhang

Article 121637

Purchase PDF Article preview

Abstract Graphical abstract

Graphical abstract

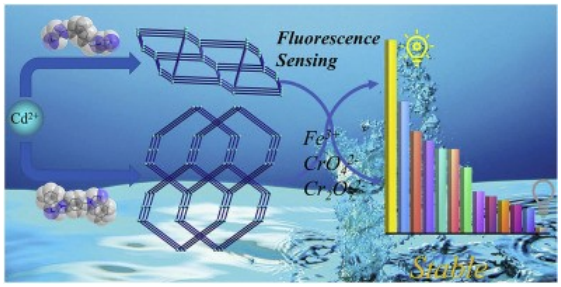

Research article ○ Abstract only

Origin of highly efficient photocatalyst NiO/$SrTiO_3$ for overall water splitting: Insights from density functional theory calculations

Yumeng Fo, Miaomiao Wang, Yanxia Ma, Hao Dong, Xin Zhou

Article 121683

Purchase PDF Article preview

Abstract Graphical abstract

Graphical abstract

NiO functions as the oxidation cocatalyst to suppress the recombination of photogenerated carriers and enhance the photocatalytic activity of $SrTiO_3$.

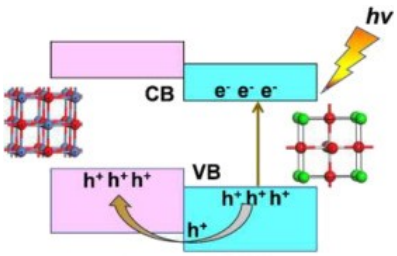

Research article ○ Abstract only

Journal of Solid State Chemistry
Supports *open access*

4.1
CiteScore

via one-pot method. The obtained product (CCM@ZIF-8&α-lip) can enhance cellular uptake and has dual pH- and GSH-responsive drug delivery system which is able to control drug release at tumor sites.

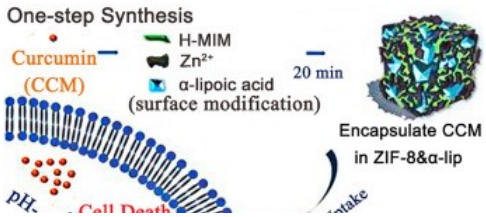

Research article ○ Abstract only

Two Cd(II)-organic frameworks for the highly luminescence sensitive detection of Cr^{VI} ions in an aqueous medium

Xin-Gang Wang, Xin Chen, Lu Zhao, Zhao-Xi Gou, ... Long Zhang

Article 121653

Purchase PDF Article preview

Abstract Graphical abstract

Graphical abstract

Two luminescent Cd(II)-organic frameworks for the highly selective sensing of Cr^{VI} ions in an aqueous medium.

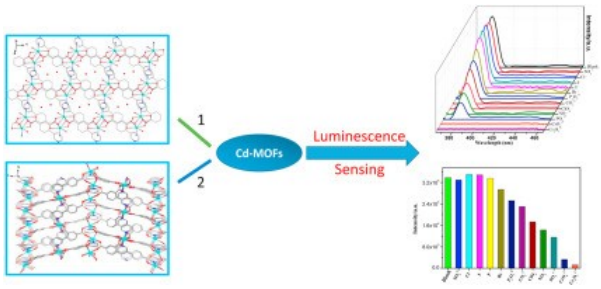

Research article ○ Abstract only

Influences of reaction temperature and pH on structural diversity of visible and near-infrared lanthanide coordination compounds based on bipyridyl carboxylate and oxalate ligands

Chao Bai, Jun-Lin Zhang, Huai-Ming Hu, Fei Wang, ... Xiaofang Wang

Article 121691

Purchase PDF Article preview

Abstract Graphical abstract

Graphical abstract

Journal of Solid State Chemistry
Supports *open access*

4.1
CiteScore

Research article ○ Abstract only

Synthesis, structure, magnetic behavior and dielectric relaxation of the $La_xSr_{2-x}Fe_xTi_{1-x}O_4$ (x = 0.5, 0.7) oxide ceramic

T.I. Chupakhina, N.V. Melnikova, N.I. Kadyrova, Yu.A. Deeva, ... R.M. Eremina

Article 121687

Purchase PDF Article preview

Abstract Graphical abstract

Graphical abstract

The dielectric constant of the $La_{0.5}Sr_{1.5}Fe_{0.5}Ti_{0.5}O_4$ ceramic sample subjected to thermobaric treatment (*c*) is much higher compared to that of the sample annealed at atmospheric pressure (*a*).

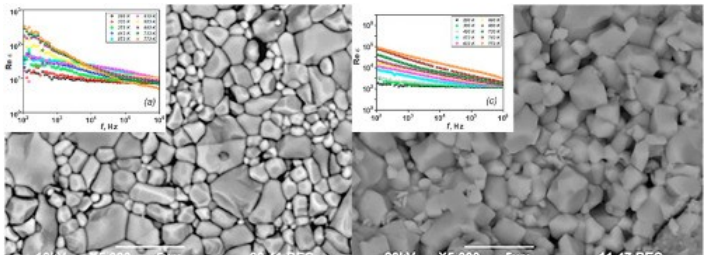

Research article ○ Abstract only

Synthesis, characterization, and redox potential properties of a new double-stranded Ni-bis(hydrazone)-based helicate

Juan D. Villada, Christian C. Carmona-Vargas, Javier Ellena, Alejandro P. Ayala, ... Manuel N. Chaur

Article 121692

Purchase PDF Article preview

Abstract Graphical abstract

Graphical abstract

A new helicate-like compound with formula $[Ni_2(bis(hydrazone))_2(Cl)_2](Cl)_2{\cdot}2H_2O$ was obtained. Cyclic voltammetry experiments were carried out to test the potential ability for catalyzing the reduction of H^+ to H_2.

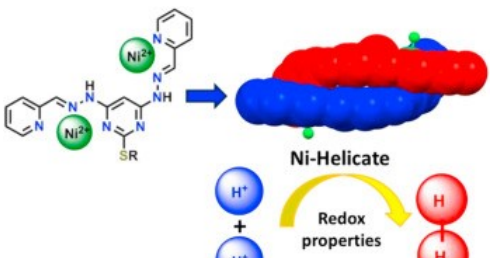

Journal of Solid State Chemistry
Supports *open access*

4.1
CiteScore

Graphical abstract

In this paper, we selected a C_2-symmetric bent diisophthalate bearing pyridine group and adenine as organic linkers, and a novel Zn-based porous MOF of $[Zn_{2.5}(dcpp)(ad)(HCOO)\cdot 3H_2O\cdot 3DMF]_n$ (**1**) was successfully synthesized. **1** contains one-dimensional channel pores with rare capsule-shaped inner cavities. Due to the high density of Lewis basic sites and open O donor sites inside the channel of the framework, activated sample **1′** exhibits considerable CO_2 and C_2H_2 storage abilities as well as highly selective separation of CO_2 and C_2H_2 over CH_4 at room temperature.

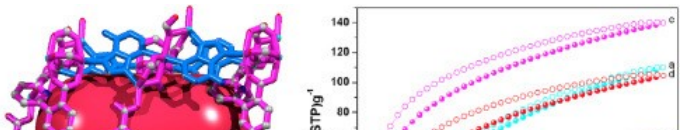

Research article ○ Abstract only

Rational design and construction of a serious of highly water-stable coordination polymers with various *N*, *N*′-donor linkers: Syntheses, diversity structures, and dye adsorption property

Chuanbin Fan, Cungang Xu, Ziao Zong, Xiaoyin Zhang, ... Yuhua Fan

Article 121673

Purchase PDF Article preview

Abstract Graphical abstract

Graphical abstract

The first author and corresponding authors made the greatest contribution to this article, while the other authors contributed similarly.

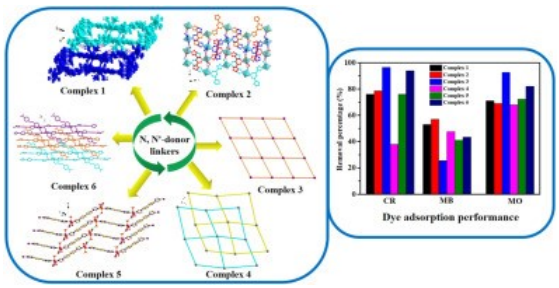

Research article ○ Abstract only

Near-infrared phosphorescence emission of three-fold interpenetrated MOF based on 1,4-bis(imidazole-1-ylmethyl)benzene: Syntheses, structure and photoelectron performance

Xin-Hong Chang, Xun-Li Ling, Xiao-Min Lu, Xiao-Gang Yang, ... Yu-Ming Guo

Article 121694

Purchase PDF Article preview

Journal of Solid State Chemistry
Supports *open access*

4.1
CiteScore

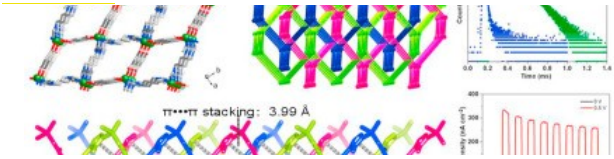

Research article ○ Abstract only

Excellent separation performance in a mesoporous MOF induced by 1D rhombic channels and bare nitrogen-donor sites

Xiao Wang, Feng-Feng Zhang, Si-Yu Li, Yue Shan Chen, ... Ji-Jiang Wang

Article 121670

Purchase PDF Article preview

Abstract Graphical abstract

Graphical abstract

Mesoporous MOFs modified by 1D channels and bare nitrogen-donor sites have been synthesized as adsorption materials with excellent adsorption and separation properties.

Research article ○ Abstract only

Cation exchange in Ni–Cu–Zn aluminate spinels revealed by EXAFS

Thanit Tangcharoen, Wantana Klysubun, Jiraroj T-Thienprasert, Chanapa Kongmark

Article 121695

Purchase PDF Article preview

Abstract Graphical abstract

Graphical abstract

The XRD and EXAFS spectra of $Ni_{1-x}Cu_xAl_2O_4$, $Cu_{1-x}Zn_xAl_2O_4$, and $Zn_{1-x}Ni_xAl_2O_4$ powders with different divalent ion concentrations showed the main translocation trends in the trivalent (Al^{3+}) and divalent (Ni^{2+}, Cu^{2+}, Zn^{2+}) ions between the tetrahedral (*A*) and octahedral (*B*) sublattices. When XRD Rietveld refinement and EXAFS curve-fitting analysis were applied, the exact crystallite size, structural parameters, and degree of inversion were obtained.

Journal of Solid State Chemistry
Supports *open access*

4.1
CiteScore

Graphical abstract

A bimetallic Co/Fe-MOF prepared by doping Fe centers into a Co-MOF structure was explored as an efficient bifunctional electrocatalyst for hydrogen evolution and oxygen evolution, which shows overpotentials of 286 and 309 mV at current densities of 10 mA cm^{-2} for HER and OER respectively. The electrolyzer by employing the Co/Fe-MOF modified Ni foam as cathode and anode shows better performance and durability for overall water splitting than the system built from commercial catalysts of Pt/C and RuO_2.

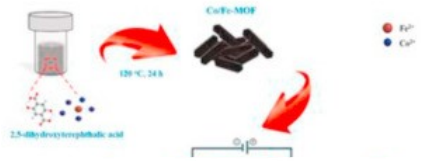

Research article ○ Abstract only

Facile synthesis of holey lamellar CuO *via* ultrasonic chemical etching toward highly efficient hydrogenation of 4-nitrophenol under mild conditions

Longlong Geng, Zhihui Lin, Zhaojun Li, Su An, ... Haixiang Han

Article 121698

Purchase PDF Article preview

Abstract Graphical abstract

Graphical abstract

A kind of holey lamellar CuO catalyst (CuO-60) with defects-rich surface, synthesized via an ultrasonic-assisted H_2O_2 etching strategy, displayed outstanding catalytic activity, stability and nearly 43 times higher efficiency than that of pristine CuO in hydrogenation of 4-nitrophenol under mild conditions.

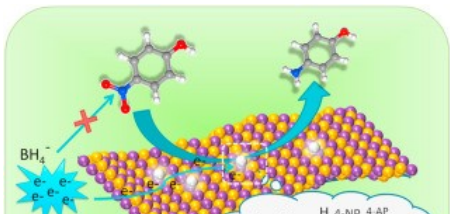

Research article ○ Abstract only

Growth of cubic anhydrous magnesium carbonate single crystal in deep eutectic solvent

Na Li, Zhidong Chang, Yifei Zhan, Hui Dang, ... Changyan Sun

Article 121684

Journal of Solid State Chemistry
Supports *open access*

4.1
CiteScore

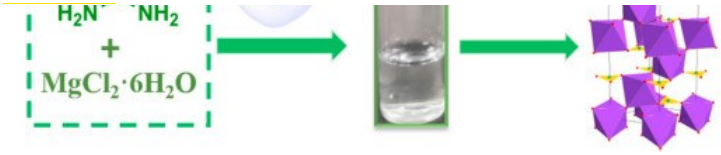

Research article ○ Abstract only

A comparison of NiO–CuO–CeO_2 composite catalysts prepared via different methods for CO oxidation

Yafei Guo, Guodong Wang, Xi Yao, Bingqian Liu

Article 121697

Purchase PDF Article preview

Abstract Graphical abstract

Graphical abstract

NiO–CuO–CeO_2 composite catalysts were prepared and applied to CO oxidation in post-fire cleanup for closed-loop air revitalization. The dual synergetic effects in solid solutions for facilitated oxygen mobility and the amorphous active metal oxides for promoted CO chemisorption were responsible for their good catalytic performance.

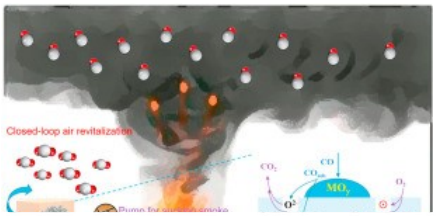

Research article ○ Abstract only

Structural characterization and electrical/electrochemical studies of $Nd_{1-x}Ba_xCo_{1-y}(Fe, Ti)_y O_{3-\delta}$ ($0 \le x \le 0.3$, $y = 0, 0.2$) materials as cathode for SOFCs application

Paramananda Jena, Dinesh Kumar, Pankaj Kumar Patro, Raja Kishora Lenka, Akhilesh Kumar Singh

Article 121682

Purchase PDF Article preview

Abstract Graphical abstract

Graphical abstract

Journal of Solid State Chemistry
Supports *open access*

4.1
CiteScore

Rui Zhao, Hong Liao, Xiurong Wu, Xueli Cao
Article 121693

Purchase PDF Article preview

Abstract Graphical abstract

Graphical abstract

The illustration of BF adsorption modes in MOF-5@SiO_2 and IRMOF-10@SiO_2 and their adsorption performance at different shell thickness.

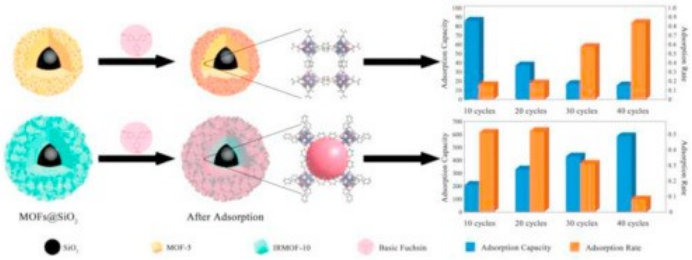

Research article ○ Abstract only

Three-dimensional homochiral coordination polymers of Eu(III) and Tb(III): Synthesis, structure determination, and optical properties

Rui-Ying Wang, Ai-Ping Huang, Wen-Bo Wang, Hong-Zhi Sun, ... Ben-Lai Wu
Article 121702

Purchase PDF Article preview

Abstract Graphical abstract

Graphical abstract

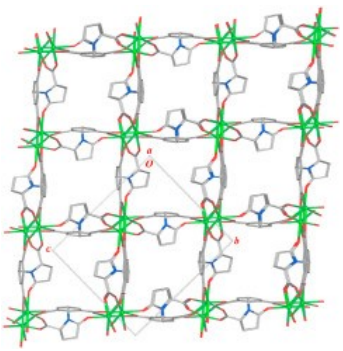

Research article ○ Abstract only

Solid-state photoluminescence, energy transfer mechanism and optical band gap of two 4f-5d complexes with 1-D chain-like

Journal of Solid State Chemistry
Supports *open access*

4.1
CiteScore

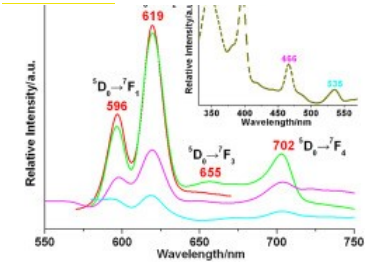

Research article ○ Abstract only

Coloured intermetallic compounds $LiCu_2Al$ and $LiCu_2Ga$

Vidyanshu Mishra, Abishek K. Iyer, Dundappa Mumbaraddi, Anton O. Oliynyk, ... Arthur Mar

Article 121703

Purchase PDF Article preview

Abstract Graphical abstract

Graphical abstract

$LiCu_2Ga$ adopts a cubic Heusler-type structure and has a yellow colour similar to gold.

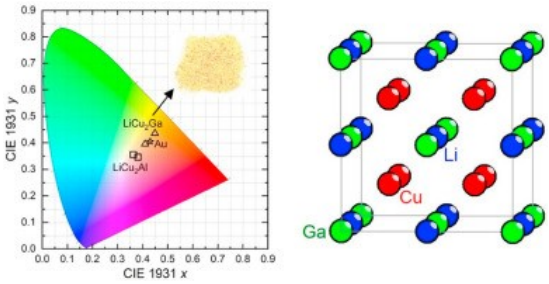

Research article ○ Abstract only

Two arsenic capped Dawson-type supramolecular hybrid assemblies induced by benzimidazole for photo-/electro-catalytic performance

Yuan Guan, Li-Ping Cui, Kai Yu, Jing-Hua Lv, ... Bai-Bin Zhou

Article 121707

Purchase PDF Article preview

Abstract Graphical abstract

Graphical abstract

Two arsenic capped Dawson arsenomolybdate supramolecular hybrid assemblies have been synthesized. Compound **1** is a 3D supramolecular

Journal of Solid State Chemistry
Supports *open access*

4.1
CiteScore

Research article ○ Abstract only

Europium metal-organic framework containing helical metal-carboxylate chains for fluorescence sensing of nitrobenzene and nitrofunans antibiotics

Shuang-Li Sun, Xi-Yu Sun, Qian Sun, En-Qing Gao, ... Wei-Jia Li

Article 121701

Purchase PDF Article preview

Abstract Graphical abstract

Graphical abstract

A 3D non-interpenetration Eu-MOF, which is composed of europium ions and quasi-rigid V-shaped carboxylate ligands *m*-phenylenediacrylic acid, shows rapid and efficient fluorescence quenching effects towards the nitrobenzene and nitrofurans antibiotics (NFAs). The sensitive identification and the visual detection of the Eu-MOF promising application as dual-functional chemosensors in the future.

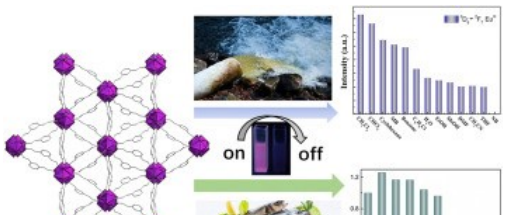

Research article ○ Abstract only

Synthesis and luminescence of $Gd_{2-x-y}Yb_xEr(Ho)_yGeMoO_8$ germanate-molibdates with scheelite structure

V.A. Krut'ko, M.G. Komova, D.V. Pominova

Article 121704

Purchase PDF Article preview

Abstract Graphical abstract

Graphical abstract

New up-conversion phosphors comprising $Gd_{2-x-y}GeMoO_8:Yb_x,Er(Ho)_y$ (GGMOs) with different concentrations of Yb and Er or Ho with tunable luminescence color were prepared using solid state and sol-gel (Pechini) methods.

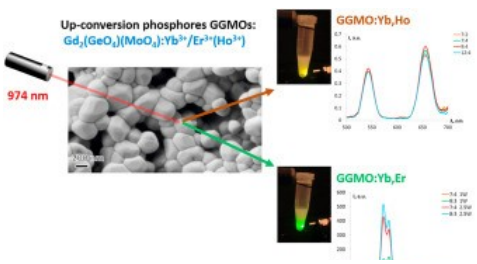

Journal of Solid State Chemistry
Supports *open access*

4.1
CiteScore

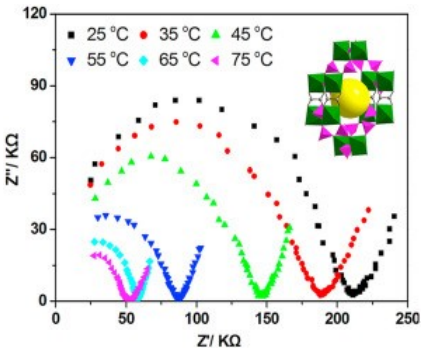

Research article ○ Abstract only

A stable Ni-based coordination polymer used as anode materials for supercapacitors

Zhikai Zhang, Lingling Gao, Jie Zhang, Xiaoyan Niu, Tuoping Hu

Article 121711

Purchase PDF Article preview

Abstract Graphical abstract

Graphical abstract

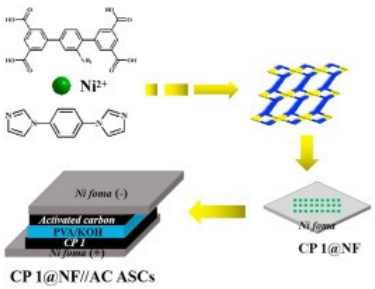

Research article ○ Abstract only

An empirical model for predicting the cell parameters of the high symmetry argyrodites

V. Sidey, A. Shteyfan

Article 121713

Purchase PDF Article preview

Abstract Graphical abstract

Graphical abstract

Comparison of the experimental and predicted cell parameters for the high symmetry argyrodites crystallizing in the space group *F-43 m*; the

Journal of Solid State Chemistry
Supports *open access*

4.1
CiteScore

Research article ○ Abstract only

Peculiarities of ion mobility and conductivity in the $(NH_4)_6LiHf_2Zr_2F_{23}$ compound

V. Ya Kavun, M.M. Polyantsev, N.N. Savchenko, A.B. Podgorbunskii, T.F. Antokhina

Article 121710

Purchase PDF Article preview

Abstract Graphical abstract

Graphical abstract

Temperature dependences of the areas of the components of ^{1}H NMR spectra belonging to ammonium ions with isotropic (a) and anisotropic (b) reorientations, and also between the number of mobile P_m and isotropically reorienting Pammoniumions vs. temperature. Insert – ^{1}H NMR spectra of the $(NH_4)_6LiHf_2Zr_2F_{23}$ at 320, 370 and 450 K.

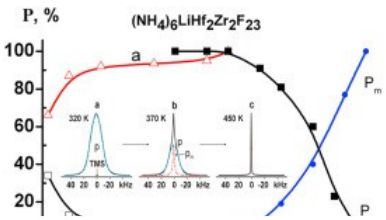

Research article ○ Abstract only

Anion replacement effect on $BaCd_2X_2$ (X = P, As, Sb, Bi) compounds: A first principles study

Syed Hatim Shah, Shamim Khan, G. Murtaza, M. Amir Ali, ... Abdullah Ali H. Ahmadini

Article 121589

Purchase PDF Article preview

Abstract Graphical abstract

Graphical abstract

The thermal conductivity of the $BaCd_2X_2$ (X= P, As, As, Bi) (a) electric part (b) phononic part. With the increase of temperature electrical part of thermal conductivity increased while phononic part of thermal conductivity decreased.

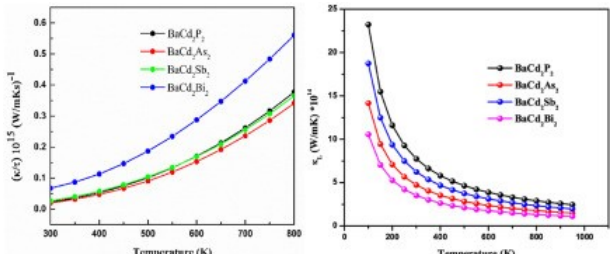

Journal of Solid State Chemistry
Supports *open access*

4.1
CiteScore

The adsorption capacity of chromium increases with pH. Moreover, the high-valence anion ion obviously increases chromium adsorption, but cation ion does not.

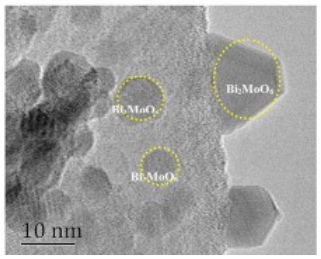

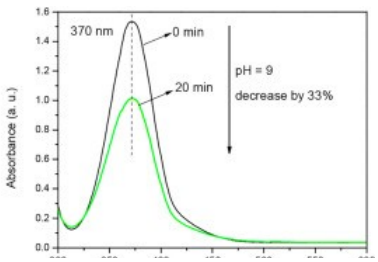

Research article ○ Abstract only

Synthesis, characterization and catalytic performance of nanocrystalline Co_3O_4 towards propane combustion: Effects of small molecular carboxylic acids

Zhao Liu, Lijun Cheng, Jia Zeng, Xin Hu, ... Yi Jiang
Article 121712

Purchase PDF Article preview

Abstract Graphical abstract

Graphical abstract

Different small molecular carboxylic acids changed the distance between Co^{2+} ions in the catalyst precursor, thus strongly affecting the structure and surface microenvironment of nanocrystalline Co_3O_4. Among them, Co_3O_4 synthesized from the cobalt citrate precursor with the largest Co^{2+} ion distance has the best catalytic activity (Co-CA: T_{90} = 250 °C).

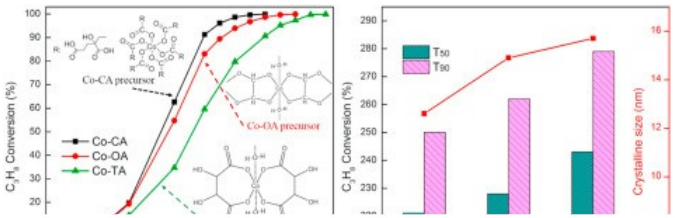

Research article ○ Abstract only

Structural variability of rare earth carboxylates based on polydentate carboxylate ligand containing pyridine group

Xiuling Xu, Zhong Wang, Chong-Chong Yan, Xiaomin Hou, Si-Fu Tang
Article 121708

Purchase PDF Article preview

Abstract Graphical abstract

Graphical abstract

Journal of Solid State Chemistry
Supports *open access*

4.1
CiteScore

Research article ○ Abstract only

A robust indium(III)–potassium(I) MOF with high CO_2/C_2- hydrocarbons over CH_4 separation performance

Tiantian Jiang, Bin Zhang, Huifang Zhou, Weize Wang, Bo Liu

Article 121726

Purchase PDF Article preview

Abstract Graphical abstract

Graphical abstract

A heterometallic indium(III)–potassium(I) MOF (**1**) has been constructed from a pyridyl-decorated tetracarboxylate organic ligand and three kinds of inorganic secondary building units, which presents an unprecedented 5-nodal (3,4,4,7,7)-connected topology. Especially, **1** possesses high chemical stability and exhibits high CO_2/C_2-hydrocarbons over CH_4 separation performance.

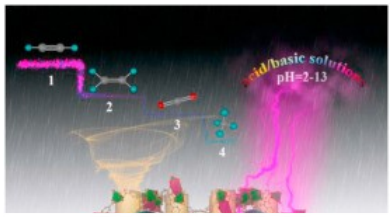

Research article ○ Abstract only

Comprehensive evaluation of formation kinetics in preparation of ternesite from different polymorphs of Ca_2SiO_4

Guojian Jing, Jinpu Zhang, Xiaolei Lu, Jiankai Xu, ... Zhengmao Ye

Article 121725

Purchase PDF Article preview

Abstract Graphical abstract

Graphical abstract

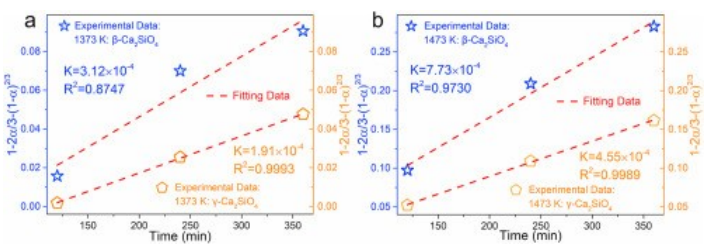

Journal of Solid State Chemistry
Supports *open access*

4.1
CiteScore

Graphical abstract

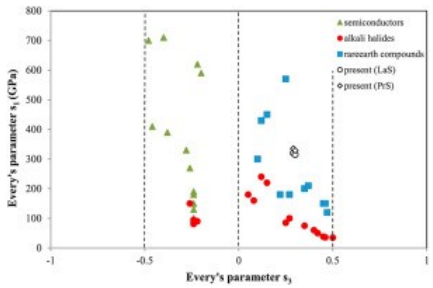

Research article ○ Abstract only

Precursor technology for the production of white and color phosphors based on Al_2O_3:Ln (Ln=Eu^{3+}, Tb^{3+} or Eu^{3+}/Tb^{3+})

I.V. Baklanova, V.N. Krasil'nikov, A.P. Tyutyunnik, Ya.V. Baklanova

Article 121699

Purchase PDF Article preview

Abstract Graphical abstract

Graphical abstract

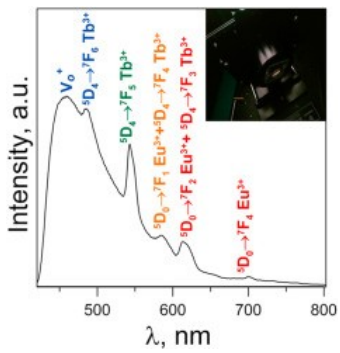

Research article ○ Abstract only

Metalloporphyrin-immobilization MOFs derived metal-nitrogen-carbon catalysts for effective electrochemical oxygen reduction

Can Huang, Huanhuan Li, Fan Liu, Enqing Liu, ... Weiping Luo

Article 121671

Purchase PDF Article preview

Abstract Graphical abstract

Graphical abstract

Journal of Solid State Chemistry
Supports *open access*

4.1
CiteScore

Research article ○ Abstract only

Enhancing photodegradation activity of g-C_3N_4 via decorating with S-doped carbon nitride quantum dots by in situ polymerization

Hongling Li, Guozhi Huang, Huazhen Xu, Zhiqing Yang, ... Yao Chen

Article 121705

Purchase PDF Article preview

Abstract Graphical abstract

Graphical abstract

The g-C_3N_4/S-CNQDs composites were synthesized by a simple in situ polymerization for the first time, integrating synthesis and doping of S-CNQDs simultaneously. Additionally, the potential mechanism of photocatalytic degradation on MO by g-C_3N_4/S-CNQDs was proposed.

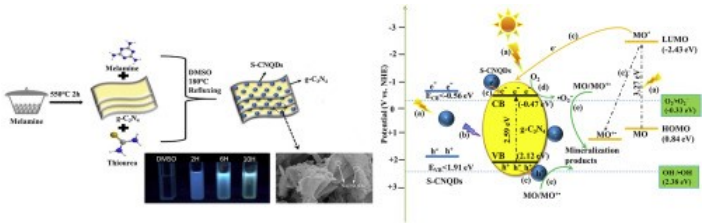

Research article ○ Abstract only

Synthesis of high quality PbS colloidal quantum dots by ultrasonic bath as photosensitizers in a TiO_2 solar cell

C. Rosiles-Perez, M.A. Serrano-Estrada, S. Sidhik, A. Alatorre-Ordaz, ... T. López-Luke

Article 121720

Purchase PDF Article preview

Abstract Graphical abstract

Graphical abstract

High quality PbS colloidal quantum dots synthesized by ultrasonic bath and their use as photosensitizers in a TiO_2 solar cell.

Journal of Solid State Chemistry
Supports *open access*

4.1
CiteScore

Graphical abstract

Noval vertically flower-like MoS_2 nanosheet decorate on N-doped graphene layers (MoS_2/N-GN) composite was prepared by a simple hydrothermal method. The MoS_2/N-GN exhibits excellent rate performance and cyclic stability benefiting from MoS_2 nanosheets and N-doped graphene.

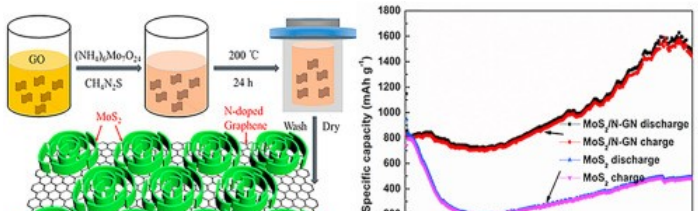

Research article ○ Abstract only

Investigation on structure, dielectric and magnetic properties of the four-layer Aurivillius phase $Pb_{1-x}Bi_{3.5+x}Nd_{0.5}Ti_{4-x}Mn_xO_{15}$ prepared via molten salt method

Zulhadjri, Tio Putra Wendari, Upita Septiani, Syukri Arief

Article 121723

Purchase PDF Article preview

Graphical abstract

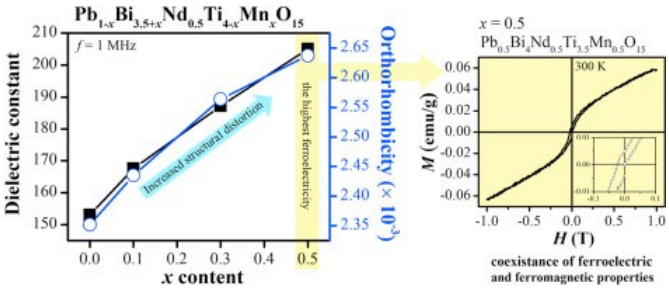

Research article ○ Abstract only

Magnetic solid phase extraction based on PVA - TEOS / grafted Fe3O4@SiO2 magnetic nanofibers for analysis of sulfamethoxazole and trimethoprim in water samples

Fatemeh Mehrabi, Maryam Mohamadi, Ali Mostafavi, Hamid Hakimi, Tayebeh Shamspur

Article 121716

Purchase PDF Article preview

Journal of Solid State Chemistry
Supports *open access*

4.1
CiteScore

Research article ○ Abstract only

Distinct role of Sn and Ge doping on thermoelectric properties in p-type $(Bi, Sb)_2Te_3$-alloys

Zhengkai Zhang, Yu Cao, Qirui Tao, Yonggao Yan, ... Xinfeng Tang

Article 121722

Purchase PDF Article preview

Abstract Graphical abstract

Graphical abstract

Doping with Sn leads to resonance states in the vicinity of the Fermi level, producing a great enhancement in power factor around 3.8 $mWm^{-1}K^{-2}$ for Sn=0.002 samples.

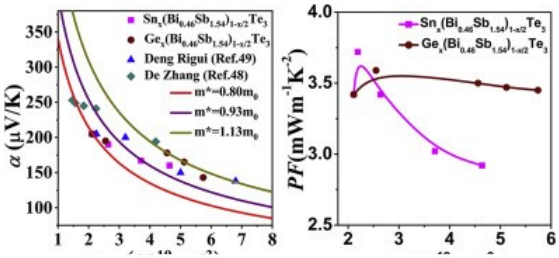

Research article ○ Abstract only

A simple phosphorylation modification of hydrothermally cross-linked chitosan for selective and efficient removal of U(VI)

Yanbing Sun, Yixiao Kang, Weihong Zhong, Yuhui Liu, Ying Dai

Article 121731

Purchase PDF Article preview

Abstract Graphical abstract

Graphical abstract

Here, novel phosphorylated hydrothermal cross-linked chitosan (HCC-PO_4) was synthesized through a simple hydrothermal method. HCC-PO_4 showed good adsorption selectivity (85.4%) and strong adsorption capacity (384.6 mg/g) for U(VI) in aqueous solution. The introduction of -PO_4 showed great advantages for adsorption. All results indicate that HCC-PO_4 is an effective adsorbent for U(VI).

Journal of Solid State Chemistry
Supports *open access*

4.1
CiteScore

Purchase PDF Article preview

Abstract Graphical abstract

Graphical abstract

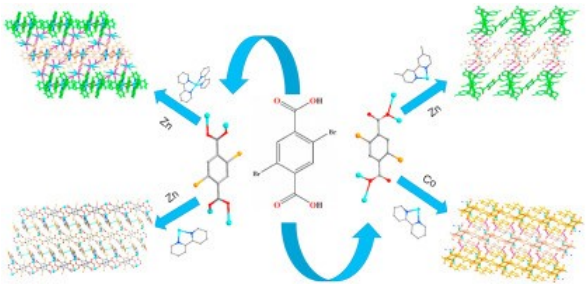

Research article ○ Abstract only

AlGaN double-walled nanotubes as ammonia gas sensor

Naiara L. Marana, Giovanne B. Pinhal, Silvia Casassa, Julio R. Sambrano

Article 121729

Purchase PDF Article preview

Abstract Graphical abstract

Graphical abstract

DFT was employed to explore the application of double-walled AlN, GaN and their alloy nanotubes as ammonia detector.

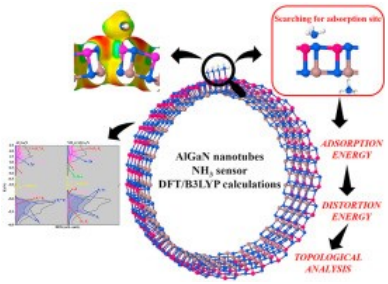

Research article ○ Abstract only

β-Cyclodextrin-functionalized mesocellular silica foams as nanocarriers of doxorubicin

Jorge L. Sánchez-Orozco, Bertha Puente-Urbina, J. Alfonso Mercado-Silva, H. Iván Meléndez-Ortiz

Article 121728

Purchase PDF Article preview

Journal of Solid State Chemistry
Supports *open access*

4.1
CiteScore

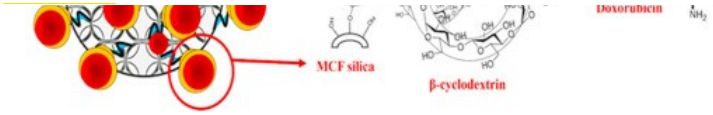

Research article ○ Abstract only

Synthesis, crystal structure and magnetic behavior of a new calcium magnesium and iron orthophosphate $Ca_2MgFe_2(PO_4)_4$

A. Ould Saleck, C. Mercier, C. Follet, O. Mentré, ... L. El Ammari

Article 121715

Purchase PDF Article preview

Abstract

Abstract

The structure of the new calcium magnesium iron orthophosphate, $Ca_2MgFe_2(PO_4)_4$ was determined from single crystal X-ray diffraction data. It crystallizes in the orthorhombic system, space group Pbca, with all atoms in general positions among which two sites are disordered. The crystal structure of this phosphate is build up from PO_4 tetrahedra linked to FeO_6 octahedra and to $(Fe/Mg)O_5$ polyhedra via common vertices. In fact, each of the two mixed sites (Fe/Mg) is surrounded by five oxygen atoms which form either a pyramid with a square base or a bi-pyramid with a triangular base. The interconnection of these polyhedra leads to a three-dimensional structure delimiting cavities where Ca^{2+} cations are localized. The powder of this compound was successfully obtained by solid state reaction and its X-ray diffraction diagram was refined by pattern matching method. The magnetic measurements show multiple transition assigned to frustrated triangles locally present in AFM (antiferromagnetic) magnetic layered units.

Research article ○ Abstract only

Efficient and selective adsorption of dye in aqueous environment employing a functional Zn(II)-based metal organic framework

Wen-bo Liu, Guan-ning Cui, Hu Wang, Dong-mei Zhang, ... Yu-hua Fan

Article 121740

Purchase PDF Article preview

Abstract Graphical abstract

Graphical abstract

A Zn-based MOF, namely $[Zn_3(\mathbf{dpcp})_2(\mathbf{1,4'\text{-}bmib})_2]_n$, highly selective and rapid adsorption of CR dyes through subtle hydrogen bonds, with an adsorption capacity of up to 262.2 mg L^{-1}.

Journal of Solid State Chemistry
Supports *open access*

4.1
CiteScore

Article 121690

Purchase PDF Article preview

Abstract Graphical abstract

Graphical abstract

The proposed mechanism for the photocatalytic CO_2 reduction to CO in PMOF /**Ru(II)**Cl_2/TEA(or TEOA)/CH_3CN system.

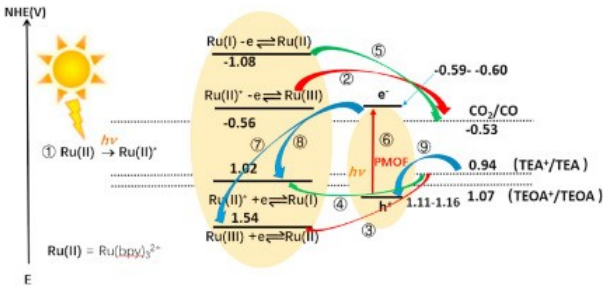

Research article ○ Abstract only

A novel white Ba3-ySryY1-x(BO3)3:xDy3+ phosphor with lower correlated color temperature and superior thermal stability

Qiang Ren, Yujing Zhao, Xiulan Wu, Jinle Zheng, ... Ou Hai

Article 121744

Purchase PDF Article preview

Abstract Graphical abstract

Graphical abstract

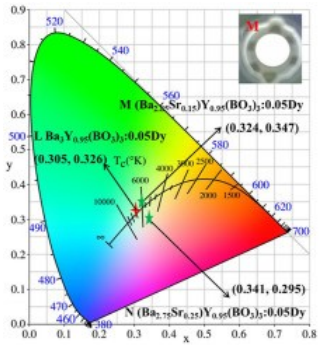

Research article ○ Abstract only

Insights into the interactions of g-C_3N_4/$LaMnO_3$ hetero-junction to their structures and electronic properties by DFT calculations

Yuzhen Fang, Xiangjin Kong, Dongting Wang, Junhai Liu, ... Shouxin Cui

Journal of Solid State Chemistry
Supports *open access*

4.1
CiteScore

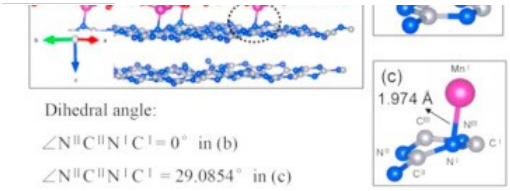

Research article ○ Abstract only

Novel two-dimensional Ga(In)$S_{1-x}Se_x$ as high-efficiency OER catalysts for photocatalytic water splitting

W.X. Zhang, C.H. Shi, C. He

Article 121730

Purchase PDF Article preview

Abstract Graphical abstract

Graphical abstract

Free energy of OER on $InS_{1-x}Se_x$ ($x = 0$) monolayer surface with three paths. For the path 1, the steps of 1, 3 and 6 are uplift and the steps of 2, 4 and 5 are decline, which indicates that the dissociation of H_2O and the generation of OOH and HOOH are more difficult. Therefore, the path 2 are selected to perform the following calculation by comparing ΔG of three pathways.

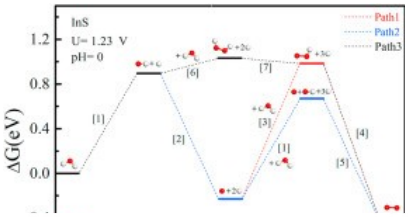

Research article ○ Abstract only

Two novel superhard monoclinic phase of B–C–N compounds

Xiaozhen Li, Mengjiang Xing

Article 121750

Purchase PDF Article preview

Abstract Graphical abstract

Graphical abstract

Journal of Solid State Chemistry
Supports *open access*

4.1
CiteScore

isomeric *N*-heterocyclic multicarboxylate ligands
Li-Na Zheng, Tao Ding, Yang-Tian Yan, Ning Xue
Article 121742

Purchase PDF Article preview

Abstract Graphical abstract

Graphical abstract

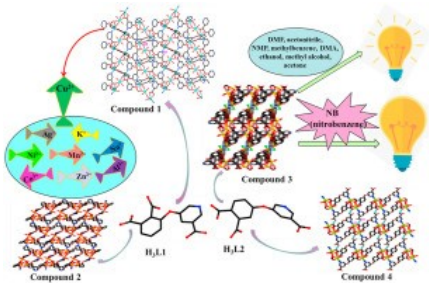

Research article ○ Abstract only

The evolution of bimetal hydroxide fragments from brucite to goethite in metal-organic frameworks for enhanced oxygen evolution reaction
Lishi Lu, Hai-Zhu Zhang, Ying Wang, Yingying Xue, ... Quan-Guo Zhai
Article 121751

Purchase PDF Article preview

Abstract Graphical abstract

Graphical abstract

Demonstrated herein a controllable evolution of bimetal hydroxide fragments in metal-organic frameworks varying from Brucite to Goethite, which promotes electron transport, exposes more active sites, and thus effectively promotes the OER performance.

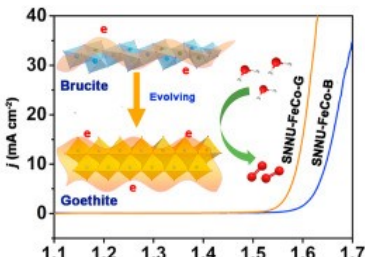

Research article ○ Abstract only

Mechanochemical synthesis and structural characterization of gallium sulfide Ga_2S_3

Journal of Solid State Chemistry
Supports *open access*

4.1
CiteScore

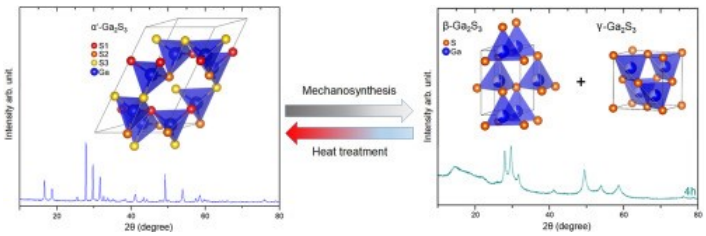

Research article ○ Abstract only

Structural, microstructural and electrical properties of $BiFeO_3$ and $BaTiO_3$ modified $Bi(Ca_{0.5}Ti_{0.5})O_3$ perovskite

Varsa Purohit, R.N.P. Choudhary

Article 121724

Purchase PDF Article preview

Abstract Graphical abstract

Graphical abstract

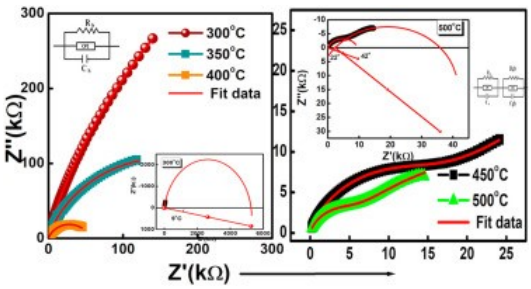

Research article ○ Abstract only

High resolution structural refinement and band gap characterization of the defect chalcopyrites $CuIn_5Te_8$, $AgIn_5Te_8$ and $AuIn_5Te_8$

Danrui Ni, Loi T. Nguyen, Elizabeth Seibel Feverston, Ruidan Zhong, Robert J. Cava

Article 121752

Purchase PDF Article preview

Abstract Graphical abstract

Graphical abstract

Charge balanced defect chalcopyrite structured compounds, AIn_5Te_8 (A = Cu, Ag, Au), are prepared and characterized. Synchrotron powder diffraction data show that the Cu and Ag analogs are tetragonal to high precision at room temperature, crystallizing in space group $I\bar{4}2m$ with

Journal of Solid State Chemistry
Supports *open access*

4.1
CiteScore

Short communication ○ Abstract only

Solid-state structural transformation of Zn(II)-bpe coordination polymers triggered by dual stimuli

Liying Zhang, Huayu Zheng, Tieqiang Wang, Xuemin Zhang, ... Yu Fu

Article 121635

Purchase PDF Article preview

Abstract Graphical abstract

Graphical abstract

Solid-state structural transformation of prepared CPs, Zn-bpe, was trigged by two environmental friendly stimuli, UV light and ozone. Moreover, these structural transformation products, L-Zn-bpe and O–Zn-bpe, maintain crystal structure of original Zn-bpe. Different structures of Zn-bpe, L-Zn-bpe and O–Zn-bpe result to different structures and distinct photocatalytic activities of their calcination products.

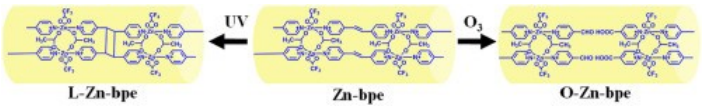

Short communication ○ Abstract only

An efficiently heterogeneous photocatalyst for degradation of cation and neutral dyes under UV light based on size-dependent effects of tetracarboxyate complex

Hai-Yun Ren, Jun-Min Du

Article 121681

Purchase PDF Article preview

Abstract Graphical abstract

Graphical abstract

A tetracarboxyate photocatalyst based on MgO6 octahedra, with its increased particle size, displayed a quenching effect as well as the lengthened emission lifetime. It might contribute to photoinduced electron–hole pairs' separation.

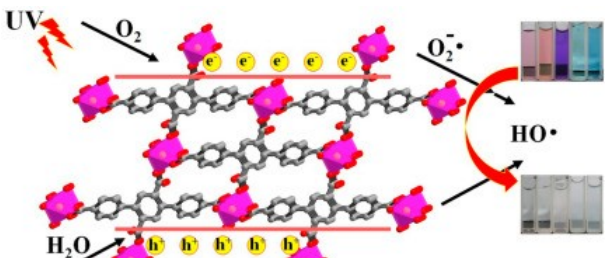

Journal of Solid State Chemistry
Supports *open access*

4.1
CiteScore

The amorphization of CeWTiOx catalyst was induced by the ionic repulsion between Ce and Ti ions (Ce^{3+}, Ce^{4+}, Ti^{3+}, Ti^{4+}) and highly oxidized W ions (W^{5+}, W^{6+}). In the tungsten-doped catalyst, the Ce–O distance decreased from 1.80 Å to 1.53 Å but the Ce–Ce distance increased from 3.52 Å to 3.83 Å. The change of the interatomic distance by amorphization lead to higher catalytic efficiency due to the increase of redox property and specific surface area.

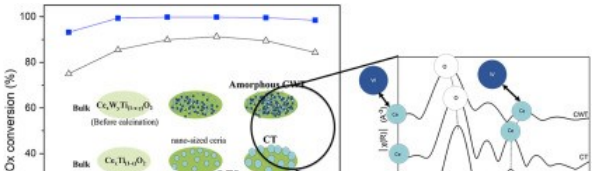

Full text access

Graphical abstract TOC continued

Article 121830

Download PDF

Journal of Solid State Chemistry 292 (2020) 121723

Contents lists available at ScienceDirect

Journal of Solid State Chemistry

journal homepage: www.elsevier.com/locate/jssc

Investigation on structure, dielectric and magnetic properties of the four-layer Aurivillius phase $Pb_{1-x}Bi_{3.5+x}Nd_{0.5}Ti_{4-x}Mn_xO_{15}$ prepared via molten salt method

Zulhadjri *, Tio Putra Wendari, Upita Septiani, Syukri Arief

Department of Chemistry, Faculty of Mathematics and Natural Sciences, Universitas Andalas, Kampus Limau Manis, Padang, 25163, Indonesia

ARTICLE INFO

Keywords:
Aurivillius phase
Molten salt method
Dielectric properties
Magnetic properties
Double-exchange interaction

ABSTRACT

In this study, the four-layer Aurivillius phases, $Pb_{1-x}Bi_{3.5+x}Nd_{0.5}Ti_{4-x}Mn_xO_{15}$ (x = 0, 0.1, 0.3, and 0.5), were prepared by the molten salt method, in order to investigate the effects on crystal structure, morphology, dielectric and magnetic properties of varying x composition. XRD patterns revealed that of the all samples were single-phase products with an orthorhombic structure. The refinement result demonstrates a compressive unit cell volume with increasing x composition. Moreover, FTIR spectroscopy showed a single mode of BO_6 octahedra, and the shifting of this mode indicates that the Mn^{3+} ions occupy the perovskite B-site. The anisotropic plate-like grain was probed by SEM, the size of which showed an increase with a higher x composition, as the proportion of Bi^{3+} increases. The dielectric properties also increase with an increasing x composition, which results from the increasing structural distortion and grain size. The investigation of the magnetic properties indicates that the ferromagnetic behavior for the $x = 0.5$ sample, presumably originated from the double-exchange interactions between Mn^{3+} and Mn^{4+} and the spin canting of distorted $Mn(1)O_6$ octahedra via the Dzyaloshinskii–Moriya interaction. The formation of the mixed-valent Mn^{3+}/Mn^{4+} could likely be caused by the oxidizing environment, produced by the oxobasicity properties of the sulfate salt in this molten-salt method. Therefore, the multiferroic properties exhibited at room temperature were due to the optimum dielectric and magnetic properties that were obtained at $x = 0.5$.

1. Introduction

For many decades, ferroelectric materials have been proposed for potential applications such as data storage devices (RAM), energy storage capacitors, piezoelectric actuators, and ultrasonic transducers, primarily due to the combination of high dielectric properties, high Curie temperatures, large remnant polarization, and low dielectric loss [1,2]. Amongst them, the Aurivillius phase with these properties has gained much interest, as compared to other alternative perovskites compound. The rapid development of these industries requires rapid continuous enhancement of material properties such as multiferroic properties, which coexist with the ferroelectric and magnetic orders, are more superior to those of memory devices, in which the data is written by the electric field, and read out by magnetization [2,3].

The Aurivillius phases have emerged as promising candidates for this multiferroic compound because of their structural flexibility which can accommodate the various A- and B-site cation substitutions. The Aurivillius phase can be described structurally as the perovskite-like layers sandwiched between the bismuth oxides layers along the c-axis and can be represented by the general formula of $(Bi_2O_2)^{2+}(A_{m-1}B_mO_{3m+1})^{2-}$. Generally, the A is a mono-, di-, or trivalent cation with dodecahedral coordination, B is a transition metal cation (d^0) with octahedral coordination, and m is the number of octahedral layers [4].

In order to combine the ferroelectric and magnetic properties in Aurivillius phases, the introduction of magnetic transition metal with a partially filled d-shell (d^n) on the B-site is a subject of many ongoing studies [5–7]. It was reported that the well-known perovskite multiferroic $BiMnO_3$ exhibits coupling between ferroelectricity and ferromagnetism [3,8,9]. Therefore, the introduction of Mn^{3+} (d^4) into the B-site perovskite was expected to give rise to the multiferroic properties. However, the contradictory character between Mn^{3+} cations (d^4) and Ti^{4+} (d^0) possibly reduced the ferroelectricity, which was associated with the high leakage current [10]. It was widely reported that the substitution of Ln^{3+} for Bi^{3+} on the A-site perovskite layers suppresses the oxygen

* Corresponding author.
E-mail address: zulhadjri@sci.unand.ac.id (Zulhadjri).

https://doi.org/10.1016/j.jssc.2020.121723
Received 7 June 2020; Received in revised form 6 August 2020; Accepted 7 September 2020
Available online 10 September 2020

vacancy concentration, decreases the leakage current density and hence enhances the dielectric and ferroelectric properties [11,12]. Therefore, it was expected that the combination of both Nd^{3+} and Mn^{3+} substitution is to obtain the multiferroic Aurivillius compound.

Recently, we have reported on the synthesis of Ca-containing four-layer Aurivillius compound ($CaBi_4Ti_4O_{15}$) with the simultaneous substitution of both Ln^{3+} and Mn^{3+}, which were obtained the single-phase products. Both series of compounds exhibited the greater structural distortion and dielectric properties with increasing x (Mn^{3+}) composition [13,14]. In this work, we explore the Pb-containing four-layer Aurivillius ($PbBi_4Ti_4O_{15}$) since the Pb^{2+} ions with $6s^2$ lone pair electrons are expected to induce a higher structural distortion, which will likely favor the higher ferroelectricity. Lead bismuth titanate, $PbBi_4Ti_4O_{15}$ ($m = 4$), adopts a non-centrosymmetric orthorhombic structure with the $A2_1am$ space group as shown in Fig. 1a. This compound exhibits the ferroelectric properties with a high Curie temperature (T_c) of 801 K. The ferroelectricity is due to the $6s^2$ lone pair electrons associated with Pb^{2+} and Bi^{3+}, which induce highly distorted BO_6 octahedra as shown in Fig. 1b [9]. However, the magnetic behavior was reported as paramagnetic.

Most of the Aurivillius phase was synthesized using a conventional solid-state method. However, this method exhibited compositional inhomogeneity owing to the Bi^{3+} volatilization at high temperatures [6]. It is also difficult to control the morphology and grain size, which in turn affects the properties of Aurivillius [15]. Recently, we have reported on the multiferroic Aurivillius phase $Pb_{0.4}Bi_{2.1}La_{0.5}Nb_{1.7}Mn_{0.3}O_9$ synthesized by the molten salt method using K_2SO_4/Na_2SO_4 salt with the varying ratios of oxide to salt [16]. The single-phase product with the best ferroelectric and ferromagnetic properties was obtained for the molar ratio of 1:7. The salt fluxes as the reaction medium provide advantages such as lower-temperature synthesis, fast ionic diffusion, and high reaction rates.

Herein, we have synthesized the compounds of composition $Pb_{1-x}Bi_{3.5+x}Nd_{0.5}Ti_{4-x}Mn_xO_{15}$ ($x = 0$, 0.1, 0.3, and 0.5) using a molten salt method using K_2SO_4/Na_2SO_4 salt, which has not previously been reported. The crystal structure, morphology, dielectric and magnetic properties were also discussed in this work.

2. Experimental procedures

The four-layer Aurivillius phases $Pb_{1-x}Bi_{3.5+x}Nd_{0.5}Ti_{4-x}Mn_xO_{15}$ ($x = 0$, 0.1, 0.3, and 0.5) were synthesized by a molten salt method using a mixture of K_2SO_4/Na_2SO_4. The starting materials used were the high purity oxides of PbO, Bi_2O_3, Nd_2O_3, TiO_2, and Mn_2O_3 (Aldrich, $\geq$ 99.9%). The molar ratios of oxide to salt were 1:7 and the synthesis temperature method were as reported in Ref. [16]. The phase formation was determined using X-ray diffraction (XRD; Shimadzu XRD 7000) with Cu Kα

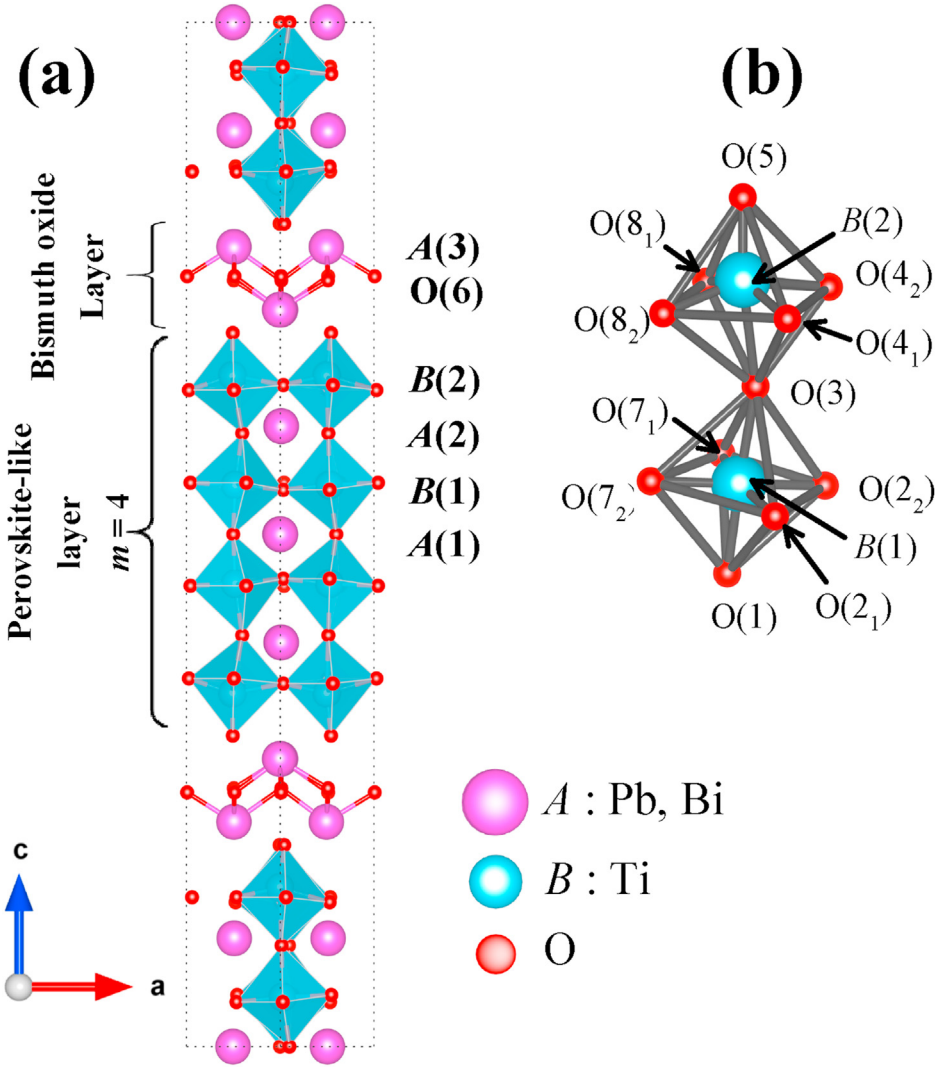

Fig. 1. (a) Crystal structure models of four-layer Aurivillius $PbBi_4Ti_4O_{15}$ phase viewed along the *ac*-plane. (b) View of distorted $B(1)O_6$ and $B(2)O_6$ octahedra projected along the c-axis. Structural parameters were taken from Ref. 9.

radiation (λ = 1.5418 Å). The Le Bail refinement method using the RIETICA program was performed to identify the crystal structure. FTIR spectroscopy was performed using a PerkinElmer 1600 FTIR spectrophotometer at room temperature. The grain morphology was observed using a scanning electron microscope (SEM; FEI INSPECT S50). The density was measured using the Archimedes method and the theoretical density was calculated from the refinement result. For the dielectric measurement, the final products were pressed into pellets with a diameter of 1 cm in and thickness 0.1 cm. The pellet sintered continuously at 500 °C and 900 °C for 3 h each. Both surfaces of sintered pellets were polished with silver conductive paste (Aldrich, 99%) to form the electrodes and dried at 423 K for 2 h. Capacitance and loss were measured as a function of frequency using a precision LCR-meter (Agilent 4980 A) with an amplitude of 1 V at 300 K. Magnetization as a function of the applied field were measured using a vibrating samples magnetometer (VSM; OXFORD 1.2H) at a temperature of 300 K.

3. Results and discussion

Fig. 2a shows the XRD patterns of $Pb_{1-x}Bi_{3.5+x}Nd_{0.5}Ti_{4-x}Mn_xO_{15}$ (x = 0, 0.1, 0.3, and 0.5) at room temperature. All XRD patterns can be well-matched with the standard XRD pattern of four-layer Aurivillius $PbBi_4Ti_4O_{15}$ (ICSD-96609). No additional peak was observed in all samples, confirming the formation of the single-phase products. This result shows that the substitution of 12.5% molar ratio La^{3+} for Bi^{3+} and 12.5% molar ratio Mn^{3+} for Ti^{4+} can be simultaneously substituted in $PbBi_4Ti_4O_{15}$ structure when the Pb:Bi ratio is adjusted accordingly. It was previously reported that the single-phase products of the four-layer Aurivillius compounds were obtained for the Mn substitution up to 15% using the molten salt method [9,13,14]. It was inferred that the substitution of Mn^{3+} for 15% could be possible.

Furthermore, the most intense diffraction peak of all samples corresponded to the (1 1 9) plane, coinciding with the (1 1 2m + 1) peak in the Aurivillius phase, whereas m = 4 refers to the number of layers. This peak gradually shifted towards the higher 2θ with an increasing x composition, as shown in the enlarged view of Fig. 2b, implying a decreased cell volume. The average crystallite size was calculated using the Scherrer equation [16]. The average crystallite size was found to decrease with an increase in x composition, which is approximately 54 nm, 52 nm, 50 nm, and 47 nm for x = 0, 0.1, 0.3, and 0.5, respectively. This result can be revealed with the increase in the full width at half maximum (FWHM) values as shown in Fig. 2c. The decreased crystallite size is correlated to the contraction of cell volume of crystal structure, as shown by the shift of the XRD peak [17].

The changes in cell parameters and cell volume were investigated by the Le Bail refinement method using the structural parameter of $PbBi_4Ti_4O_{15}$ with a space group $A2_1am$ as an initial model [9]. Le Bail fits to the XRD patterns of $Pb_{1-x}Bi_{3.5+x}Nd_{0.5}Ti_{4-x}Mn_xO_{15}$ are shown in Fig. 3. The good fit between the experimental and calculated patterns with a small difference between these two intensities demonstrates that all samples adopt the orthorhombic $A2_1am$ space group and this structure does not change with the varying x composition.

The refined lattice parameters and cell volume is shown in Fig. 4. The a lattice parameter slightly increase, whereas the b and c lattice parameters decrease as x composition increases, leading to the decrease in cell volume. Referring to the ionic radius of Pb^{2+} (1.49 Å) and Bi^{3+} (1.31 Å) for 12-fold coordination and the ionic radii of Mn^{3+} (0.645 Å) and Ti^{4+} (0.605 Å) for 6-fold coordination [18,19], the decreased cell volume is strongly affected by the increasing proportion of smaller Bi^{3+} and the decreasing proportion of larger Pb^{2+}, according to the nominal formula of $Pb_{1-x}Bi_{3.5+x}Nd_{0.5}Ti_{4-x}Mn_xO_{15}$. These compositional changes resulted in the higher distortion of the BO_6 octahedra, by which the structure becomes more orthorhombic [20,21]. This distortion led to the tilting of BO_6 octahedra along the a-axis, confirmed by the increased difference between the a and b lattice parameter [22]. The degree of distortion could be evaluated from the orthorhombicity ratio $(a-b)/(a+b)$. The orthorhombicity gradually increased with increasing x composition as shown in Fig. 4b, which revealed the increase in structural distortion. This is also consistent with the decrease in the tolerance factor (t) calculated for the perovskite-part structure [23]. The increase in distortion was driven both by the increase of $6s^2$ lone pair electrons of Bi^{3+} and the size mismatch between the A- and B-site cations [24,25]. The increase in distortion contributes to the increased ferroelectricity.

Furthermore, it is clearly observed in Fig. 4a that the c parameter decreased abruptly with the cell volume for x = 0.5. A decreased c parameter is generally associated with a shortening of the B–O bond distance as well as the BO_6 octahedra size. The significant decrease of c parameter in x = 0.5 might be further raised by the formation of smaller Mn^{4+} ions (0.54 Å) compared to Mn^{3+} (0.645 Å). A similar trend was also observed in $Ca_{1-x}Bi_{3+x}LaTi_{4-x}Mn_xO_{15}$, whereas the formation of Mn^{4+} caused a decrease in c lattice parameters and volume cell [14]. The existence of Mn^{4+} ions could also be expected to give rise to the magnetic ordering, as discussed further below.

Fig. 5a shows the IR spectra of $Pb_{1-x}Bi_{3.5+x}Nd_{0.5}Ti_{4-x}Mn_xO_{15}$ in the spectral range 600–1400 cm^{-1}, corresponding to the vibration modes of BO_6 octahedra (>200 cm^{-1}). A vibration mode at ~830 cm^{-1} was

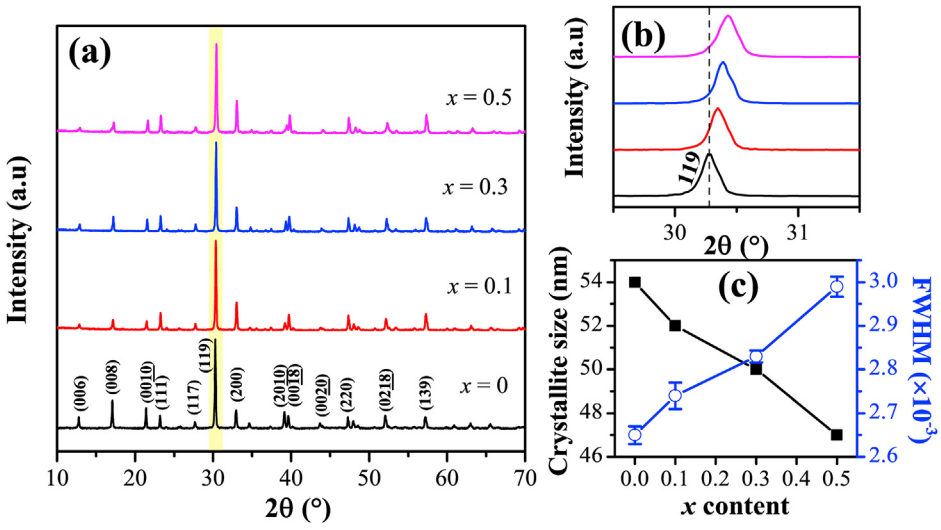

Fig. 2. (a) XRD patterns of $Pb_{1-x}Bi_{3.5+x}Nd_{0.5}Ti_{4-x}Mn_xO_{15}$ powders (x = 0, 0.1, 0.3, and 0.5). (b) The enlarged view of (1 1 9) XRD peak. (c) Comparison of crystallite size and FWHM peak.

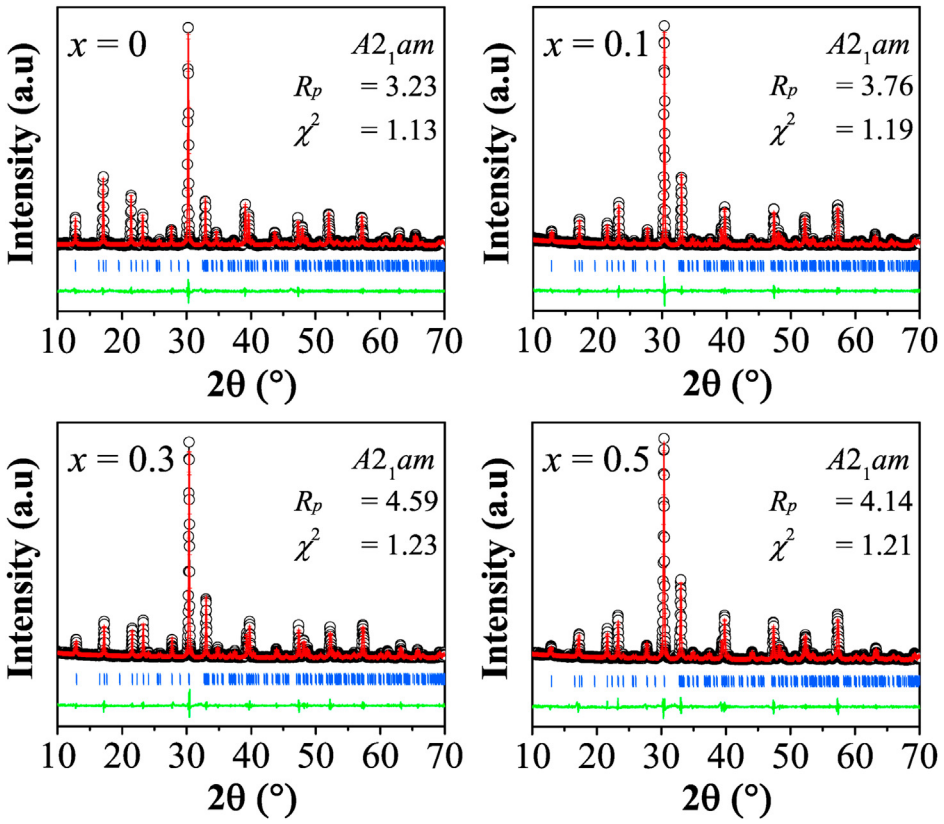

Fig. 3. Le Bail fits to XRD data for single-phase $Pb_{1-x}Bi_{3.5+x}Nd_{0.5}Ti_{4-x}Mn_xO_{15}$ and the reliability factor of refinement result. Observed XRD data (open circles), calculated data (red line), difference data (green line), and Bragg reflections of space group $A2_1am$ (blue tick). (For interpretation of the references to colour in this figure legend, the reader is referred to the Web version of this article.)

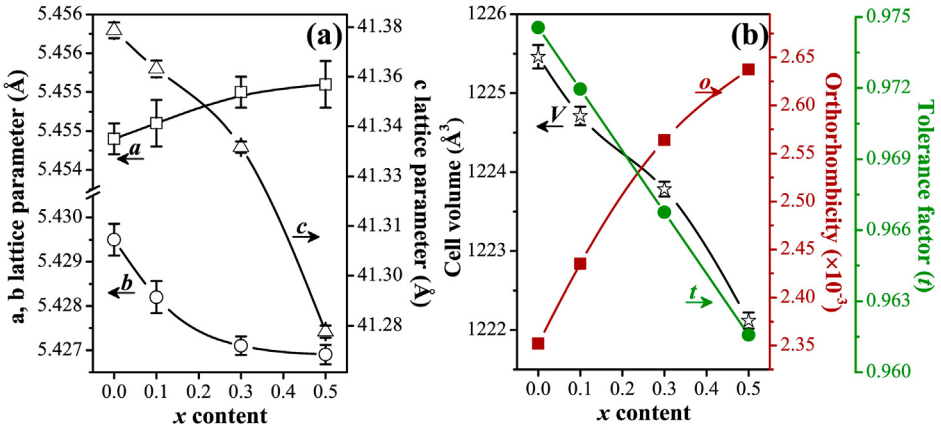

Fig. 4. (a) Refined lattice parameters of $Pb_{1-x}Bi_{3.5+x}Nd_{0.5}Ti_{4-x}Mn_xO_{15}$ (x = 0, 0.1, 0.3, 0.5). (b) Composition dependence of cell volume, orthorhombicity ratio and tolerance factor.

observed in the spectra of all samples, assigned to the symmetric *B*–O stretching mode of BO_6 octahedra in the perovskite layers [11]. The peak position and the full widths at half maximum (FWHM) of the IR spectra fitted using a Lorentzian model are shown in Fig. 5b. It was found that the peak shifted towards the lower wavenumber and became broader with the increase in x composition. The obvious shift of *B*–O mode was induced by the substitution of Mn^{3+} for Ti^{4+} since the chemical bond strength of the Mn–O bond (362 kJ/mol) is smaller than that of Ti–O (666.5 kJ/mol) [20,26]. The increase in FWHM value correlated to the increased compositional disorder of the *B*-site cations as the proportion of Mn^{3+} increased. Moreover, no traces of sulfate vibration mode around 970–995 cm^{-1} reveals that the salt does not chemically react with the product of this method.

SEM micrographs of $Pb_{1-x}Bi_{3.5+x}Nd_{0.5}Ti_{4-x}Mn_xO_{15}$ powder sample were shown in Fig. 6a-d. The typical plate-like grains of the Aurivillius phase were observed. The plate-like morphology was formed due to the lower surface energy along the (00*l*) planes, which lead to the preferential grain growth along the *a*–*b* plane [11]. The grain size was observed to increase with increasing x composition. The increase in grain size was associated with an increase in the proportion of Bi^{3+} since it has high ionic mobility and stimulates grain growth [20]. Fig. 6e shows that the density increased as x composition increased. The relative density of all samples were found to be greater than ~94% of the theoretical density, indicating the well-dense grains under this molten salt method.

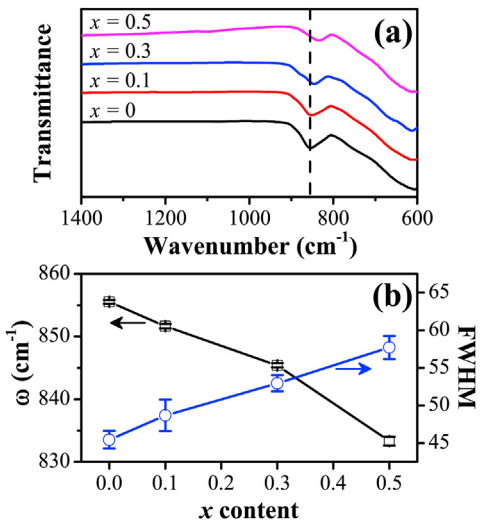

Fig. 5. (a) FTIR spectra of $Pb_{1-x}Bi_{3.5+x}Nd_{0.5}Ti_{4-x}Mn_xO_{15}$ ($x = 0$, 0.1, 0.3, 0.5) at room temperature. (b) Composition dependence of wavenumber and FWHM of *B*–O vibration mode.

Fig. 7 shows the dielectric constant (ε) and dielectric loss (tan δ) measured over various frequency ranges at room temperature (300 K). It was observed that the dielectric constant decreased as the frequency increased and became constant at high frequencies, which is typical behavior of ferroelectric materials [27]. At low frequencies, the contribution of different polarizations (*i.e.* dipolar, ionic, electronic, and space-charge) led to the higher dielectric constant. This was also caused by the accumulation of charge carriers at both surface and grain boundaries since it could not respond well to the applied field, also known as the Maxwell-Wagner effect [9]. Therefore, the stronger dispersion of dielectric constant with increasing *x* composition is likely due to the domination of the space-charge polarizations, arising from the increase in electron concentration of Mn ions [10,11]. Thus, the high dielectric constant at low frequencies arises from the combination of both intrinsic and extrinsic factors.

The decrease in dielectric constant at higher frequencies was due to the absence of different types of polarization and the conducting behavior. Thus, the magnitude of the dielectric constant at high frequencies is more reliable to reflect the intrinsic polarizability. The dielectric constant at 1 MHz was found to increase from 105.5 for $x = 0$ to 174.6, 200.8, and 245.1, respectively for the increase in *x* composition. The high dielectric constant at room temperature was associated with the ferroelectric behavior in all samples, which correlated to the $A2_1am$ orthorhombic symmetry. The increased ferroelectricity was attributed to the increased structural distortion, as revealed by the increasing orthorhombicity ratio and the decreasing tolerance factor (*t*). Besides, the increase in grain size allowed the domain to be polarized more easily, which also contributed to this magnitude [7,16].

The dielectric loss (tan δ) also exhibited a strong dispersive value at low frequencies as seen in Fig. 7b, which is due to the domination of space charge polarization effects. The dielectric loss at 1 MHZ was found to increase for $x = 0$, 0.1, 0.3, and 0.5 with value of 0.017, 0.057, 0.111, and 0.291, respectively, indicating the sample became more conductive. This was strongly affected by the increase in the electron concentration as the charged carriers by the substitution of Mn^{3+} for Ti^{4+}. Furthermore, the reduction in the number of grain boundaries subsequently contributed to the higher dielectric loss since it allowed easier electron migration [20].

To investigate the magnetic behavior, the magnetic field dependence of the magnetization (*M-H*) was performed at room temperature as shown in Fig. 8. The magnetic behavior was compared only for sample $x = 0$ and $x = 0.5$ since the sample of $x = 0.5$ exhibited the highest dielectric properties of these series and the maximum Mn composition was expected to provide the highest magnetic properties. The *M-H* curve of $x = 0$ exhibited a negative magnetization with no loop opening, demonstrating a typical diamagnetic behavior [7]. The $x = 0.5$ sample exhibited a non-linear fashion, and a narrow hysteresis loop can be observed in the inset of Fig. 8, indicating the existence of ferromagnetic behavior. The unpaired electrons of Mn cations were mainly responsible for the magnetic properties of $x = 0.5$. The unsaturated hysteresis loop indicated that the maximum applied magnetic field of 1 T was insufficient to completely arrange the spin orders. The saturated magnetization (M_s) and the remnant saturation (M_r) were 0.058 emu/g and 0.005 emu/g, respectively.

The ferromagnetism of $x = 0.5$ possibly originated from the existence of the double-exchange interactions in BO_6 octahedra. As shown in Fig. 1a, the four-layer Aurivillius phases contain two types of octahedral structures as the inner $B(1)O_6$ and the outer $B(2)O_6$, where the Mn^{3+} cations possibly occupy in both sites. It was previously reported that the magnetic transition cations preferentially occupy the inner site of $B(1)O_6$ octahedra with a lower distortion due to the high symmetry of the *d*-orbitals [5,9]. This preference for local ordering of magnetic ions was also observed previously by Raman spectroscopy [6,20]. Therefore, it can be inferred that Mn ions preferred to occupy the adjacent inner $B(1)O_6$ octahedra in this sample. Moreover, it has commonly been observed that

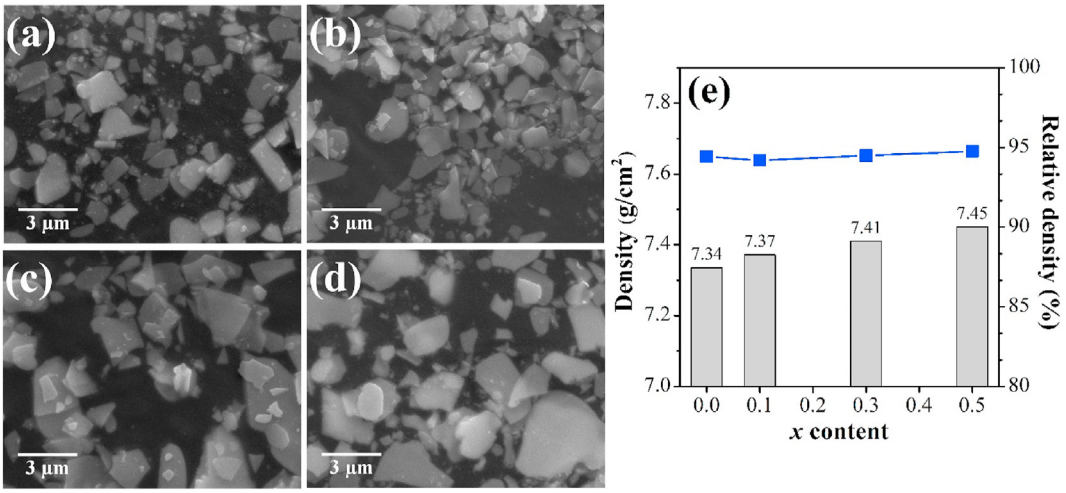

Fig. 6. SEM micrograph of $Pb_{1-x}Bi_{3.5+x}Nd_{0.5}Ti_{4-x}Mn_xO_{15}$ powders samples (a) $x = 0$ (b) $x = 0.1$ (c) $x = 0.3$ (d) $x = 0.5$ and (e) the density and relative density as a function of *x* composition.

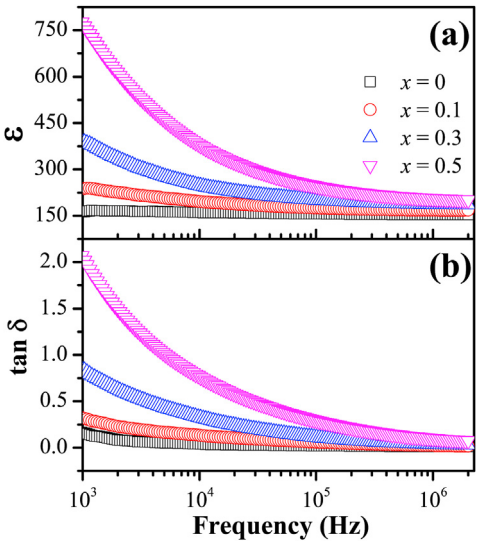

Fig. 7. (a) Dielectric constant (ϵ) and (b) dielectric loss (tan δ) of $Pb_{1-x}Bi_{3.5+x}Nd_{0.5}Ti_{4-x}Mn_xO_{15}$ ($x = 0$, 0.1, 0.3, and 0.5) as a function of frequency at room temperature.

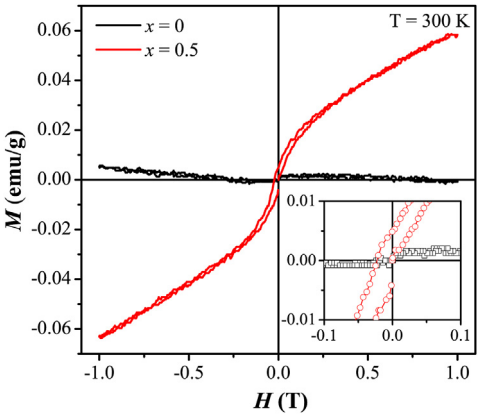

Fig. 8. *M–H* loops of $Pb_{1-x}Bi_{3.5+x}Nd_{0.5}Ti_{4-x}Mn_xO_{15}$ ($x = 0$ and 0.5) measured at room temperature. The inset graph denotes the enlarged part of *M–H* loops under the low field.

the combination of mixed-valent magnetic cations in equal ratio enable the double-exchange interaction to take place [6,10]. The possibility of Mn ions to form the multiple valence states of Mn^{3+}/Mn^{4+} further allows the existence of this interaction. As the molten-salt method was used, the formation of Mn^{4+} ions might be due to the oxide ion donor mechanism involving oxobasic SO_4^{2-} anions from sulfate salts, as explained by Lux-Flood acid-base theory [16,28]. The oxidation of Mn^{3+} is further promoted by the oxygen-rich environment during the high-temperature calcination. The formation of mixed-valent Mn^{3+}/Mn^{4+} in equal proportions was previously reported in Aurivillius compounds synthesized using the molten salt method [9,27]. Thus, the $x = 0.5$ might also contain that Mn^{3+} and Mn^{4+} since it was synthesized using the same molar ratio [16]. The existence of Mn^{4+} ions was in good agreement with the decreased *c* parameter in the refinement result. For the following reasons, we speculate that the possible double-exchange interactions occurring within Mn-rich clusters in the inner $B(1)O_6$ octahedra via Mn(1)-O(1)-Mn(1) bonds, gave rise to the ferromagnetic behavior.

These phenomena were also observed in the four-layer Aurivillius $Pb_{0.4}Bi_{4.6}Ti_{3.4}Mn_{0.6}O_{15}$ resulting in the presence of ferromagnetic interactions with the ferromagnetic-paramagnetic transition temperature (T_c) at 21.49 K [9]. Interestingly, in this sample $Pb_{0.5}Bi_4Nd_{0.5}Ti_{3.5}Mn_{0.5}O_{15}$, the ferromagnetic behavior is still observed at room temperature (300 K), which indicates the improved magnetic properties with the substitution of Nd^{3+} cations for 0.5 mol. It is reported that the ferromagnetic interaction is also correlated with the spin canting of the magnetic ions via the antisymmetric Dzyaloshinskii-Moriya (DM) interaction [29]. According to the recent studies, this spin canting effects can be achieved by substitution of Ln^{3+} cation with a smaller ionic radius on the *A*-site, leading to the smaller bond angles and shorter bond length and hence the enhanced magnetic properties [30,31]. Compared with the $Pb_{0.4}Bi_{4.6}Ti_{3.4}Mn_{0.6}O_{15}$ compound, the substitution of smaller Nd^{3+} (1.27 Å) for Bi^{3+} (1.31 Å) in our current sample induce a higher distortion and a shorter bond length of $Mn(1)O_6$ octahedra, which likely favor enhanced magnetic properties. This result confirms that the combination of *A*- and *B*-site cation substitution is a feasible way to enhance the dielectric as well as the magnetic properties in the Aurivillius phase. We noted that the above discussion is preliminary and requires further study to reveal the magnetic mechanism.

4. Conclusions

The single-phase of the four-layer Aurvillius $Pb_{1-x}Bi_{3.5+x}Nd_{0.5}Ti_{4-x}Mn_xO_{15}$ ($x = 0$, 0.1, 0.3 and 0.5) was successfully obtained by the molten salt method using K_2SO_4/Na_2SO_4 fluxes. The structural analysis confirmed that all the samples adopted the non-centrosymmetric orthorhombic symmetry with the $A2_1am$ space group and the cell volume decreased as the *x* composition increased. The FTIR spectra indicated that the Mn^{3+} ions occupied the *B*-site of perovskite layers. The anisotropic plate-like grain morphology was observed for all samples. The dielectric constant increased with increasing *x* composition, which indicated the increase in ferroelectricity. The ferroelectric polarization arises mainly from the displacement of the *A*- and *B*-site cation along the *a*-direction, according to the orthorhombic $A2_1am$ symmetry. The magnetic investigation for the highest Mn-composition sample ($x = 0.5$) indicated a ferromagnetic behavior, which is assumed to arise from the double-exchange involving the short-range Mn^{3+}-*O*-Mn^{4+} bonds in the inner *B* $(1)O_6$ octahedra structure. The best dielectric properties were obtained for $x = 0.5$ sample, which was at 1 MHz and RT provided a maximum dielectric constant of 245.1 and a dielectric loss (tan δ) of 0.291. This sample also exhibited the ferromagnetic behavior with the remnant magnetization (M_r) of 0.005 emu/g at RT. The coexistence of ferroelectricity and ferromagnetism with the simultaneous substitution of Nd^{3+} and Mn^{3+} for $PbBi_4Ti_4O_{15}$ was expected to provide a potential multiferroic material for the applications in memory storage devices.

CRediT authorship contribution statement

Zulhadjri: Conceptualization, Methodology, Writing - original draft, Validation. **Tio Putra Wendari:** Investigation, Visualization, Writing - original draft. **Upita Septiani:** Investigation, Formal analysis. **Syukri Arief:** Writing - review & editing.

Declaration of competing interest

The authors declare that they have no known competing financial interests or personal relationships that could have appeared to influence the work reported in this paper.

Acknowledgments

This work was supported by the Ministry of Research, Technology and Higher Education (RISTEKDIKTI) of the Republic of Indonesia through the Fundamental Grant with contract number 051/SP2H/LT/DRPM/2019.

References

[1] J.F.Scott, Ferroelectric Memories, first ed., Springer-Verlag Berlin Heidelberg, New York, n.d. doi:10.1007/978-3-662-04307-3.

[2] W. Eerenstein, N.D. Mathur, J.F. Scott, Multiferroic and magnetoelectric materials, Nature 442 (2006) 759–765, https://doi.org/10.1038/nature05023.

[3] A.J.C. Buurma, G.R. Blake, T.T.M. Palstra, Multiferroic Materials : Physics and Properties, Elsevier Ltd., 2016, https://doi.org/10.1016/B978-0-12-803581-8.09245-6.

[4] B. Aurivillius, Mixed bismuth oxides with layer lattices 1. The structure type of $CaNb_2Bi_2O_9$, Ark. För Kemi. 1 (1949) 463–480.

[5] Y. Shu, Q. Ma, Z. Ding, L. Cao, X. Chen, F. Yang, X. Zeng, Multiferroic behaviors of Co-doped $Bi_4NdTi_3FeO_{15}$ ceramics, Phys. Lett. 383 (2019) 911–914, https://doi.org/10.1016/j.physleta.2018.12.031.

[6] R. Ti, C. Wang, H. Wu, Y. Xu, C. Zhang, Study on the structural and magnetic properties of Fe/Co co-doped $Bi_4Ti_3O_{12}$ ceramics, Ceram. Int. 45 (2019) 7480–7487, https://doi.org/10.1016/j.ceramint.2019.01.040.

[7] Z. Yin, Y. Sheng, G. Ma, Dielectric, multiferroic and magnetodielectric properties of Co/Fe co-doped – $Bi_4Ti_3O_{12}$ ceramics, J. Mater. Sci. Mater. Electron. 30 (2019) 10483–10490, https://doi.org/10.1007/s10854-019-01391-0.

[8] C.C. Chou, C.L. Huang, S. Mukherjee, Q.Y. Chen, H. Sakurai, A.A. Belik, H.D. Yang, Multiple magnetic transitions in multiferroic $BiMnO_3$, Phys. Rev. B 80 (2009) 184426, https://doi.org/10.1103/PhysRevB.80.184426.

[9] Zulhadjri, B. Prijamboedi, A.A. Nugroho, N. Mufti, A. Fajar, T.T.M. Palstra, Ismunandar, Aurivillius phases of $PbBi_4Ti_4O_{15}$ doped with Mn^{3+} synthesized by molten salt technique: structure , dielectric , and magnetic properties, J. Solid State Chem. 184 (2011) 1318–1323, https://doi.org/10.1016/j.jssc.2011.03.044.

[10] Y. Shi, Y. Pu, J. Li, W. Wang, R. Shi, M. Yang, X. Guo, X. Wang, J. Ji, X. Peng, Q. Zhang, L. Guo, Dielectric, optical, and multiferroic properties of Co-doped $SrBi_2Nb_{1.8}Fe_{0.2}O_9$ ceramics, J. Mater. Sci. Mater. Electron. 31 (2020) 4719–4731, https://doi.org/10.1007/s10854-020-03028-z.

[11] A. Khokhar, P.K. Goyal, O.P. Thakur, A.K. Shukla, K. Sreenivas, Influence of lanthanum distribution on dielectric and ferroelectric properties of $BaBi_{4-x}La_xTi_4O_{15}$ ceramics, Mater. Chem. Phys. 152 (2015) 13–25, https://doi.org/10.1016/j.matchemphys.2014.11.074.

[12] L. Sheng, X. Du, Q. Chao, P. Zheng, W. Bai, L. Li, F. Wen, W. Wu, L. Zheng, Enhanced electrical properties in Nd and Ce co-doped $CaBi_4Ti_4O_{15}$ high temperature piezoceramics, Ceram. Int. 44 (2018) 18316–18321, https://doi.org/10.1016/j.ceramint.2018.07.044.

[13] Zulhadjri, J.I. Bilian Sahiga, W.T. Putra, Emriadi, Synthesis and structural analysis of aurivillius phase, $Ca_{1-x}Bi_{3+x}NdTi_{4-x}Mn_xO_{15}$, Res. J. Chem. Environ. 22 (2018).

[14] Zulhadjri, A.A. Billah, T.P. Wendari, Emriadi, U. Septiani, S. Arief, Synthesis of aurivillius phase $CaBi_4Ti_4O_{15}$ doped with both La^{3+} and Mn^{3+} cations: crystal structure and dielectric properties, Mater. Res. 23 (2020), e20190521, https://doi.org/10.1590/1980-5373-MR-2019-0521.

[15] H. Chen, B. Shen, J. Xu, L. Kong, J. Zhai, Correlation between grain sizes and electrical properties of $CaBi_2Nb_2O_9$ piezoelectric ceramics, J. Am. Ceram. Soc. 95 (2012) 3514–3518, https://doi.org/10.1111/j.1551-2916.2012.05327.x.

[16] T.P. Wendari, S. Arief, N. Mufti, J. Baas, G.R. Blake, Zulhadjri, Ratio effect of salt fluxes on structure, dielectric and magnetic properties of La,Mn-doped $PbBi_2Nb_2O_9$ Aurivillius phase, Ceram. Int. 46 (2020) 14822–14827, https://doi.org/10.1016/j.ceramint.2020.03.007.

[17] S. Chandel, P. Thakur, M. Tomar, V. Gupta, A. Thakur, Investigation of structural, optical, dielectric and magnetic studies of Mn substituted $BiFeO_3$ multiferroics, Ceram. Int. 43 (2017) 13750–13758, https://doi.org/10.1016/j.ceramint.2017.07.088.

[18] R.D. Shannon, Revised effective ionic radii and systematic studies of interatomie distances in halides and chaleogenides, Acta Crystallogr. 32 (1976) 751–767.

[19] J. Tellier, P. Boullay, M. Manier, D. Mercurio, A comparative study of the Aurivillius phase ferroelectrics $CaBi_4Ti_4O_{15}$ and $BaBi_4Ti_4O_{15}$, J. Solid State Chem. 177 (2004) 1829–1837, https://doi.org/10.1016/j.jssc.2004.01.008.

[20] T.P. Wendari, S. Arief, N. Mufti, V. Suendo, A. Prasetyo, J. Baas, G.R. Blake, Zulhadjri, Synthesis, structural analysis and dielectric properties of the double-layer Aurivillius compound $Pb_{1-2x}Bi_{1.5+2x}La_{0.5}Nb_{2-x}Mn_xO_9$, Ceram. Int. 45 (2019) 17276–17282, https://doi.org/10.1016/j.ceramint.2019.05.285.

[21] J. Yuan, R. Nie, Q. Chen, D. Xiao, J. Zhu, Structural distortion, piezoelectric properties, and electric resistivity of A-site substituted Bi_3TiNbO_9-based high-temperature piezoceramics, Mater. Res. Bull. 115 (2019) 70–79, https://doi.org/10.1016/j.materresbull.2019.03.019.

[22] A.B. Missyul, I.A. Zvereva, T.T.M. Palstra, A.I. Kurbakov, Double-layered Aurivillius-type ferroelectrics with magnetic moments, Mater. Res. Bull. 45 (2010) 546–550, https://doi.org/10.1016/j.materresbull.2010.02.002.

[23] D.Y. Suárez, I.M. Reaney, W.E. Lee, Relation between tolerance factor and Tc in Aurivillius compounds, J. Mater. Res. 16 (2001) 3139–3149, https://doi.org/10.1557/JMR.2001.0433.

[24] Ismunandar, B.A. Hunter, B.J. Kennedy, Cation disorder in the ferroelectric Aurivillius phase $PbBi_2Nb_2O_9$: an anamolous dispersion X-ray diffraction study, Solid State Ionics 112 (1998) 281–289, https://doi.org/10.1016/S0167-2738(98)00222-7.

[25] S.M. Blake, M.J. Falconer, M. Mccreedy, P. Lightfoot, Cation disorder in ferroelectric Aurivillius phases of the type $Bi_2ANb_2O_9$ (A=Ba, Sr, Ca), J. Mater. Chem. 7 (1997) 1609–1613.

[26] Y. Luo, Comprehensive Handbook of Chemical Bond Energies, first ed., CRC Press, Boca Raton, 2007 https://doi.org/10.1201/9781420007282.

[27] T.P. Wendari, S. Arief, N. Mufti, A. Insani, J. Baas, G.R. Blake, Zulhadjri, Structural and multiferroic properties in double-layer Aurivillius phase $Pb_{0.4}Bi_{2.1}La_{0.5}Nb_{1.7}Mn_{0.3}O_9$ prepared by molten salt method, J. Alloys Compd. 820 (2020) 153145, https://doi.org/10.1016/j.jallcom.2019.153145.

[28] J. Boltersdorf, N. King, P.A. Maggard, Flux-mediated crystal growth of metal oxides: synthetic tunability of particle morphologies, sizes, and surface features for photocatalysis research, CrystEngComm 17 (2015) 2225–2241, https://doi.org/10.1039/c4ce01587h.

[29] S. Liu, S. Yan, H. Luo, L. Yao, Z. Hu, S. Huang, L. Deng, Enhanced magnetoelectric coupling in La-modified $Bi_5Co_{0.5}Fe_{0.5}Ti_3O_{15}$ multiferroic ceramics, J. Mater. Sci. 53 (2018) 1014–1023, https://doi.org/10.1007/s10853-017-1604-6.

[30] Z. Yu, X. Meng, Z. Zheng, Y. Lu, H. Chen, C. Huang, H. Sun, K. Liang, Z. Ma, Y. Qi, T. Zhang, Room temperature multiferroic properties of rare-earth-substituted Aurivillius phase $Bi_5Ti_3Fe_{0.7}Co_{0.3}O_{15}$ ceramics, Mater. Res. Bull. 115 (2019) 235–241, https://doi.org/10.1016/j.materresbull.2019.04.002.

[31] J. Li, Y. Pu, X. Wang, Y. Shi, R. Shi, M. Yang, W. Wang, X. Guo, X. Peng, Effect of yttrium doping on the structure, dielectric multiferroic and magnetodielectric properties of $Bi_5Ti_3FeO_{15}$ ceramics, J. Mater. Sci. Mater. Electron. 31 (2020) 4345–4353, https://doi.org/10.1007/s10854-020-02992-w.